

Achieving over 90 % initial Coulombic efficiency and highly stable Li storage in SnO₂ by constructing interfacial oxygen redistribution in multilayers

Xuexia Lan

School of Materials Science and Engineering, Guangdong Provincial Key Laboratory of Advanced Energy Storage Materials, South China University of Technology, Guangzhou, 510640, China

Jie Cui

Analytical and Testing Center, South China University of Technology, Guangzhou, 510640, China

Xiaofeng Zhang

Department of Physics, OSED, Key Laboratory of Low Dimensional Condensed Matter Physics (Department of Education of Fujian Province), Jiujiang Research Institute, Xiamen University, Xiamen, 361005,

Renrong Hu (✉ msrenronghu@scut.edu.cn)

School of Materials Science and Engineering, Guangdong Provincial Key Laboratory of Advanced Energy Storage Materials, South China University of Technology, Guangzhou, 510640, China

<https://orcid.org/0000-0002-8994-6438>

Liang Tan

School of Materials Science and Engineering, Guangdong Provincial Key Laboratory of Advanced Energy Storage Materials, South China University of Technology, Guangzhou, 510640, China

Jiayi He

School of Materials Science and Engineering, Guangdong Provincial Key Laboratory of Advanced Energy Storage Materials, South China University of Technology, Guangzhou, 510640, China

Houpo Zhang

School of Materials Science and Engineering, Guangdong Provincial Key Laboratory of Advanced Energy Storage Materials, South China University of Technology, Guangzhou, 510640, China

Xingyu Xiong

School of Materials Science and Engineering, Guangdong Provincial Key Laboratory of Advanced Energy Storage Materials, South China University of Technology, Guangzhou, 510640, China

Xianfeng Yang

Analytical and Testing Centre, South China University of Technology

Shunqing Wu

Department of Physics, OSED, Key Laboratory of Low Dimensional Condensed Matter Physics (Department of Education of Fujian Province), Jiujiang Research Institute, Xiamen University, Xiamen, 361005,

Min Zhu

SCUT

Article

Keywords: Conversion reaction, interface engineering, tin dioxide, built-in electric field, oxygen redistribution

Posted Date: March 11th, 2021

DOI: <https://doi.org/10.21203/rs.3.rs-243641/v1>

License:  This work is licensed under a Creative Commons Attribution 4.0 International License.

[Read Full License](#)

1 **Achieving over 90 % initial Coulombic efficiency and highly stable Li storage in**
2 **SnO₂ by constructing interfacial oxygen redistribution in multilayers**

3
4 Xuexia Lan^{†a}, Jie Cui^{†b}, Xiaofeng Zhang^{†c}, Renzong Hu^{*a}, Liang Tan^a, Jiayi He^a,
5 Houpo Zhang^a, XingYu Xiong^a, Xianfeng Yang^b, Shunqing Wu^{*c}, and Min Zhu^{*a}

6
7 ^a School of Materials Science and Engineering, Guangdong Provincial Key
8 Laboratory of Advanced Energy Storage Materials, South China University of
9 Technology, Guangzhou, 510640, China

10 ^b Analytical and Testing Center, South China University of Technology, Guangzhou,
11 510640, China

12 ^c Department of Physics, OSED, Key Laboratory of Low Dimensional Condensed
13 Matter Physics (Department of Education of Fujian Province), Jiujiang Research
14 Institute, Xiamen University, Xiamen, 361005, China

15 [†] These authors contributed equally.

16 * Corresponding Author.

17 E-mail addresses: msrenzonghu@scut.edu.cn (Renzong Hu)

18 wsq@xmu.edu.cn (Shunqing Wu)

19 memzhu@scut.edu.cn (Min Zhu)

20

21

1 **Abstract:**

2 Among the promising high capacity anode materials, tin dioxide (SnO_2) represents
3 a classic and important candidate that involves both conversion and alloying reactions
4 toward Li storage. However, the inferior reversibility of conversion reactions usually
5 results in low initial Coulombic efficiency (ICE, $\sim 60\%$), small reversible capacity
6 and poor cycling stability of electrodes. Here, we demonstrate that by carefully
7 designing the interface structure of SnO_2 -Mo, a breakthrough comprehensive
8 performance with ultrahigh average ICE up to 92.6 %, large capacity of 1067 mA h
9 g^{-1} and 100 % capacity retention after 200 cycles can be realized in a multilayer
10 Mo/ SnO_2 /Mo electrode. The amorphous SnO_2 /Mo interfaces, which are induced by
11 redistribution of oxygen atoms between SnO_2 and Mo, can precisely adjust the
12 reversible capacity and cycling stability of the multilayers, while the stable capacities
13 of electrodes are parabolic with the interfacial density. Theoretical calculations and
14 in/ex-situ experimental investigation clearly reveal that oxygen redistribution in the
15 SnO_2 /Mo hetero-interfaces boosts the Li ions transport kinetics by inducing a built-in
16 electric field and improves the reaction reversibility of SnO_2 . This work provides a
17 new understanding of the interface-performance relationship of metal-oxide hybrid
18 electrodes and pivotal guidance for creating high performance Li-ion batteries.

19

20 **Keywords:** Conversion reaction; interface engineering; tin dioxide; built-in electric
21 field; oxygen redistribution

1 **1 Introduction**

2 The increasing demand on higher energy density and safety for Li ion batteries
3 (LIBs) make it extremely important to exploit new anode materials with large capacity,
4 safe operating potentials and fast Li^+ diffusion kinetics in substituting the
5 conventional graphite anodes.¹⁻³ The past considerable efforts have verified that many
6 alloying-type metals/semiconductors (Sn, Al, Si, Ge, etc.) and conversion-type metal
7 oxides (Co_3O_4 , Fe_2O_3 , MnO_2 , etc.) meet well the criteria of higher capacity and safer
8 potentials toward Li storage but still suffer from unsatisfactory reversibility and
9 stability.^{4,5} Among those, tin dioxide (SnO_2) anode, storing Li^+ through a combination
10 of conversion reaction ($\text{SnO}_2 + 4\text{Li}^+ + 4\text{e}^- \rightarrow \text{Sn} + 2\text{Li}_2\text{O}$) and then alloying reaction
11 ($\text{Sn} + 4.4\text{Li}^+ \rightarrow \text{Li}_{4.4}\text{Sn}$), with a theoretical capacity of 1494 mA h g^{-1} and moderate
12 lithiation potential range of 0.4-1.0 V vs. Li/Li^+ ,^{6,7} has been regarded as one of the
13 typical and important anode materials for both mechanism exploring and performance
14 tuning toward Li storage, which could ensure larger energy density and a higher level
15 of safety for the cells.^{8,9} However, the following mentioned two major drawbacks of
16 metal and metal oxide anodes have seriously impeded the wide utilization of it: (1) the
17 large initial irreversible capacity loss characterized by low initial Coulombic
18 efficiency (ICE) mainly due to inferior reversibility of conversion reaction,^{10, 11} (2)
19 severe capacity fading and unstable electrode/electrolyte interfaces resulted from the
20 large volume effect of active phases during continuous cycling.¹²

21 With respect to the reverse conversion reactions, Sn is oxidized to SnO_2 by
22 obtaining O from the decomposed Li_2O . As the Li_2O and SnO_2 have very similar

1 formation enthalpy (-598 kJ mol^{-1} for Li_2O and -581 kJ mol^{-1} for SnO_2),^{6, 13} how Sn
2 competes with Li to capture O in the electrode is the key to tuning the reversible
3 conversions of Li_2O to SnO_2 . In fact, it has been revealed that the grain size of Sn and
4 its contact area with Li_2O determined the amount of regenerated SnO_2 , and high
5 reversibility of conversion reactions can be achieved by reducing the size of Sn to
6 about 10 nanometers.^{14, 15} However, the nanosized Sn grains formed in the lithiated
7 SnO_2 tend to coarsen, which is driven by minimizing the interface energy between the
8 Sn and Li_2O which are immiscible, and becomes serious at room temperature due to
9 the extremely low recrystallization temperature ($\sim -53 \text{ }^\circ\text{C}$) of Sn.^{16, 17} Thus, the
10 kinetics of the reverse conversion reaction is impeded and the transformation of a
11 fraction of Sn to Li_xSn or SnO_2 is also hindered within large particles.¹⁸ These suggest
12 that both the reversibility and stability of electrochemical reactions in SnO_2 electrodes
13 are very sensitive to the interface interactions among the active phases including Sn,
14 Li_xSn and Li_2O . Therefore, it is important to stabilize the nanostructure of SnO_2 to
15 maintain high reversibility of conversion reaction, and this has been achieved by
16 pinning the grain boundary with the addition of transition metals (TM: Mn, Fe, Co,
17 etc.), which leads to a high ICE of more than 77 % and enhanced capacity retention in
18 ternary SnO_2 -TM-C composites.^{16, 18, 19}

19 It has been noted that adding TM not only has the effect of dramatically
20 decreasing the Sn coarsening tendency within Li_2O matrix, but also favors the
21 combination of TM with O at the SnO_2 /TM hetero-interface which results in the
22 redistribution of O and the formation of vacancy (O_{vac}) in SnO_2 .¹⁸ The introduction of

1 O_{vac} in semiconductor can reduce the band gap to enhance intrinsic conductivity, and
2 influence the surface thermodynamics of semiconductor oxides and thus facilitate
3 phase transition,^{20, 21} which both promote the reversibility of conversion reactions in
4 SnO_2 -TM hybrids.¹⁸ Besides, recent studies have also demonstrated that strong
5 chemical bonding within heterogeneous interfaces, especially the metal/
6 semiconductor interfaces, could lead to internal charge redistribution and even
7 structural changes that favor the formation of a built-in electric field, boosting
8 interfacial charge transfer.²²⁻²⁴ Inspired by these, to enable a breakthrough in
9 comprehensive performance for SnO_2 -based anodes, i.e., achieving simultaneously
10 high ICE, large capacity and superior cycling stability, rational constructing interfacial
11 interactions to boost the O redistribution for forming more vacancies in SnO_2 -TM
12 system should be an effective way.

13 In this work, we carefully design the interfacial structure between SnO_2 and Mo
14 to modulate the structural configuration and oxygen distribution by tuning the
15 SnO_2 -Mo multilayers. Most surprisingly, we find that the redistribution of O atoms
16 occurs at the hetero-interfaces between active SnO_2 and inactive Mo layers,
17 generating amorphous interface regions which can precisely adjust the reversible
18 capacity and cycling stability. A remarkable comprehensive performance with
19 ultrahigh average ICE up to 92.6 % and superior capacity retention of 100 % after 200
20 cycles can be achieved in a sandwiched Mo/ SnO_2 /Mo electrode. In addition, a
21 combination of DFT calculations and in/ex-situ experimental analysis reveals the
22 mechanism of capacity increase and fast Li^+ transport kinetics by SnO_2 /Mo interfaces

1 with the introduction of interfacial O redistribution, which provides a new
2 understanding on the interface-performance relationship of metal-oxide hybrid
3 electrode materials for the rational design of high-performance LIBs.

4 **2 Results and discussion**

5 **2.1 Highly reversible, stable, and rapid charge transfer process in SnO₂-Mo** 6 **multilayer electrodes**

7 The as-sputtered SnO₂-Mo multilayer films were directly used as binder-free
8 anodes for LIBs (Supplementary Fig. 1). For simplicity, all of the tested anodes are
9 abbreviated as listed in Supplementary Table 1, including their preparation parameters.
10 Fig. 1a, b present the reversible capacity and ICEs of the SnO₂, Mo/SnO₂ (MS),
11 SnO₂/Mo (SM) and Mo/SnO₂/Mo (MSM) films at a current density of 0.2 mA cm⁻²
12 within 0.01-3.0 V vs. Li/Li⁺. Compared to the pure SnO₂ electrode, both the reversible
13 capacity and ICEs can be greatly increased for the electrodes combined with Mo layer.
14 Notably, the symmetric sandwich structured MSM electrode exhibits the best
15 comprehensive electrochemical performance, achieving an ultrahigh average ICE of
16 92.6 %, large initial reversible capacity of 1067 mA h g⁻¹ (calculated based on the total
17 mass of the sputtered layers including Mo layers), with ~100% capacity retention after
18 200 cycles. In contrast, the ICEs of SnO₂, MS, and SM electrodes are 75.0 %, 83.9 %
19 and 85.8 %, respectively. To eliminate the effect of total film thickness on the stability
20 of large capacity, MSM/5 (5 layers) and MSM/11(11 layers) electrodes
21 (Supplementary Fig. 1 and Supplementary Table 1) were tested respectively with the

1 same layer thickness. As displayed in Supplementary Fig. 2, both the MSM/5 and
2 MSM/11 electrodes, with total film thickness of approximately 700 nm and 1800 nm,
3 respectively (Supplementary Fig. 3), also deliver ICEs greater than 90 % and maintain
4 stable high capacities of more than 1000 mA h g⁻¹ throughout the cycles. These
5 consolidate that the good reversibility and stability of electrochemical reactions are
6 intrinsic for the SnO₂/Mo multilayer electrodes regardless of its film nature.

7 Obviously, the SnO₂/Mo multilayer structure greatly benefits the Li storage
8 performance. It is believed that the SnO₂/Mo interface plays a key role, and thus,
9 further interface tuning was carried out based on the MSM electrode. By taking
10 constant film electrode thickness, MSM-A, MSM-B and MSM-C electrodes were
11 prepared to have different layer numbers and consequently different interfacial
12 densities (Supplementary Fig. 1 and Supplementary Table 1). The interfacial density
13 is defined as the ratio of the total thickness of the interfaces to the total thickness of
14 the SnO₂ layers in the electrodes, and the thickness of interface is taken as 14 nm
15 according to cross sectional transmission electron microscopy (TEM) observation
16 shown in Fig. 3 later. As shown in Fig. 1c, they exhibit different reversible capacities
17 although good cycling stability is maintained for all the MSM, MSM-A, MSM-B and
18 MSM-C electrodes. Among them, the MSM-B achieves the highest initial charge
19 capacity of more than 1700 mA h g⁻¹ while remaining high ICE of 93.4 %
20 (Supplementary Fig. 4). Thus, the interfaces between SnO₂ and Mo layers have
21 significant impacts on electrochemical reactions and Li storage capability.
22 Supplementary Fig. 5 shows the differential charge capacity plots (DCPs) for the

1 SnO₂, MSM and MSM-B electrodes. There are two distinct groups of peaks, including
2 the peaks of Li_xSn dealloying within 0.01-1.0 V and the broad peaks of reversed
3 conversion reaction within 1.0-2.0 V. These three electrodes in Supplementary Fig. 5
4 maintain similar peak intensity for the dealloying reactions. Nevertheless, compared
5 to pure SnO₂ electrode, the reversibility of conversion reaction is greatly improved for
6 the MSM, and it can be further enhanced in the MSM-B with a much higher
7 interfacial density, demonstrating that the interfacial effect plays a huge role in
8 adjusting the electrochemical reactions of SnO₂-Mo multilayers. Fig. 1d illustrates the
9 relationship between the capacity increase and the interfacial density of multilayers
10 with a constant thickness as the MSM. The fitting curve reveals that the charge
11 capacity increase is parabolic with the interfacial density, and it reaches the maximum
12 as the interfacial density reaches the optimal value (about 0.5, representing half of the
13 SnO₂ layer is interfacial status), indicating that the additional reversible capacity
14 should be contributed from the interfacial Li storage. Continuing to increase the
15 interfacial density, the reversible capacity gradually decreases until it reaches the
16 lowest value in MSM-E and MSM-n with an interfacial density of 1 (The electrode is
17 entirely interfacial). The detailed mechanism will be further discussed later. This fitted
18 curve clearly demonstrates the interfacial regulation on the electrochemical reactions
19 and Li storage, and provides pivotal guidance for creating high performance
20 SnO₂-based electrodes. Fig. 1e summarizes the electrochemical performance reported
21 in the representative literatures on SnO₂-based anodes.²⁵⁻⁴⁶ From the perspective of
22 large reversible capacity, high ICE and superb capacity retention, the MSM electrode

1 represents a breakthrough comprehensive performance for SnO₂-based anodes.^{14, 18, 47}

2 Since the interfaces in SnO₂-Mo electrodes have an obvious regulatory effect on
3 the reversible storage of Li, it must also affect the charge transfer process. To evaluate
4 the Li storage characteristic and the transport kinetics, the rate capabilities of the
5 MSM and SnO₂ electrodes are compared at various current rates from 0.05 to 2 mA
6 cm⁻², as shown in Fig. 2a. Apparently, the MSM exhibits higher capacity retention
7 than SnO₂ at any current rate. More importantly, as it switches from high rate of 2 mA
8 cm⁻² to 0.05 mA cm⁻² again, the capacity of MSM recovers to that in the initial cycle
9 at 0.05 mA cm⁻². The superior rate capability of MSM indicates the significantly
10 increased Li⁺ transport kinetics within both the SnO₂ and Mo layers. Fig. 2b shows
11 the discharge/charge curves at the 1st and 50th cycle for the SnO₂, MSM and MSM-B.
12 The initial charge curves reveal that MSM has a reversible capacity 1.4 times that of
13 SnO₂, and the reversible capacity of MSM-B is up to 1.6 times that of MSM. Due to
14 the inactivity of the Mo layers, the additional capacity for the electrodes with greater
15 interfacial density should originate from the Li storage reactions at the interfaces
16 mainly within the potential range of 1.0-2.0 V, which will be further verified later.

17 Fig. 2b also reveals that the initial reversible capacities of MSM and MSM-B can
18 still be maintained or even slightly increased after 50 cycles, which could be
19 attributed to the Li storage reactions at the SnO₂/Mo interfaces and gradually
20 activation of active materials, as well as the decomposition of solid electrolyte
21 interphase (SEI) at high potential range above 2.0V. In contrast, the capacity of SnO₂
22 has drastically decreased. Generally, most of the capacity fading in SnO₂ electrode

1 results from the declining reversibility of the conversion reaction ($\text{Li}_2\text{O} + \text{Sn} \rightarrow$
2 SnO_2), which can be reflected by the variation of differential charge capacity plots
3 (DCPs) at different cycles.^{14, 18} As shown in Fig. 2c, in the SnO_2 electrode, the
4 dealloying peaks of Li_xSn around 0.5 V gradually shift to higher potentials due to
5 increasing polarization resulted from the coarsening of Sn and Li_xSn phases.
6 Furthermore, the complete disappearance of DCP peaks within 1.0-2.0 V after 50
7 cycles suggests dramatically declining reversibility of conversion reactions in the
8 SnO_2 electrode. In contrast, for the MSM, as shown in Fig. 2d, both the potential
9 positions and integral intensities of these DCP peaks remain stable even after 200
10 cycles, demonstrating the outstanding reversibility and stability of the alloying and
11 conversion reactions.

12 **2.2 Phase and structural characterization for the interfaces and O redistribution** 13 **in MSM electrode**

14 Fig. 3a displays the grazing incidence X-ray diffraction (GI-XRD) patterns taken
15 from the MSM with different incident angles, exhibiting structural information along
16 the film depth. The phase constituents of each layer were tested by adjusting the
17 grazing angle. Fig. 3b displays the comparison of GI-XRD patterns with the same
18 incident angle of 2° for the MSM, MSM-A, MSM-B and MSM-C. Obviously, the
19 diffraction peaks gradually weaken and broaden towards a lower angle as the
20 SnO_2/Mo interfacial density increased, implying the increased amorphous components
21 and defects such as oxygen vacancies,^{48, 49} and another distinguishable diffraction

1 peak at 44° could be MoO_x .

2 The cross-sectional morphology of different SnO_2 -Mo multilayers with obvious
3 columnar crystal feature was visually confirmed by scanning electron microscope
4 (SEM) and TEM images in Supplementary Figs. 6-9. Specifically, Fig. 3c shows the
5 cross-sectional structure of the MSM sample prepared by focused ion beam (FIB),
6 which consists of two layers of Mo and one layer of SnO_2 . The high-resolution TEM
7 (HRTEM) images and selected area electron diffraction (SAED) patterns demonstrate
8 the detailed structural information on each layer and the interface (Fig. 3d-f). The
9 lattice fringes and diffraction rings reveal that most Mo and SnO_2 are polycrystalline.
10 Nevertheless, there are some amorphous components around the columnar Mo grains,
11 as depicted in Fig. 3d. Meanwhile, from the HRTEM and fast Fourier transform (FFT)
12 images for the interface between SnO_2 and Mo layers (Fig. 3f), it is revealed that there
13 is an amorphous region along the SnO_2 /Mo interface with a width of about 14 nm.
14 Moreover, as shown in Supplementary Fig. 9g, amorphous products are more
15 prominent in the MSM-B with greater interfacial density, which is consistent with the
16 results in Fig. 3b. By comparing energy-dispersive X-ray spectroscopy (EDS)
17 mapping and line scan of Sn, Mo, and O elements for the MSM electrode, as shown in
18 Fig. 3g, it can be found that Mo layer and SnO_2 layer have obvious mutual diffusion
19 across the interface in the MSM. O shows a high content in the Mo layer, although it
20 mainly exists in the SnO_2 layer. For MSM-B with higher interfacial density (Fig. 3h),
21 O is more uniformly distributed across the multilayers, meaning the even more
22 evident diffusion of O. These indicate that increasing the interfacial density among

1 SnO₂ and Mo layers can induce obvious O redistribution and thus amorphous region
2 formation, which could be the main reason for the great enhancements in the capacity,
3 reversibility and cycling stability of the MSM and MSM-B electrodes.

4 Such a redistribution of O could result in the phase transformation at the
5 SnO₂/Mo interfaces. The detachment of O atoms from the lattice of SnO₂ definitely
6 also introduces abundant defects, i.e. O_{vac}. To further verify that, the chemical
7 information at the interfaces of MSM and the presence of O_{vac} were analyzed using
8 X-ray photoelectron spectroscopy (XPS). Fig. 4a, b show the XPS spectra for Sn and
9 Mo elements at the up side of interface in MSM, the two peaks in Mo 3d XPS
10 spectrum confirm the presence of MoO₃, while the valence band spectrum of Sn
11 belongs to SnO. Similarly, for the down side of interface (Fig. 4c, d), the Mo3d XPS
12 spectrum can be fitted into six peaks, corresponding to Mo, MoO₂ and MoO₃,
13 respectively, and the valence band spectrum of Sn can be assigned to the combination
14 of SnO and SnO₂. The existence of SnO and MoO₂ as well as MoO₃ in the MSM
15 electrode reveals a significant redistribution of O and the resulting O_{vac} in SnO₂ layer.
16 The presence of the O_{vac} in MSM is further proved by O 1s XPS spectra in
17 Supplementary Fig. 10. The peaks at 530.3 eV and 531.7 eV are attributed to the
18 Metal (M)–O and the O_{vac}, respectively.^{20, 50} Thus, the O redistribution and O_{vac} here
19 due to interfacial effects reflects the charge transfer and structural change in MSM,
20 leading to the generation of the amorphous interfaces and the amorphous MoO_x
21 products in Mo layers, and affecting the electronic and structural behaviors of MSM
22 electrode, thereby modifying its reaction kinetics and therefore improving the Li

1 storage capabilities.

2 To verify the specificity and superiority of the O redistribution and in situ formed
3 amorphous interfaces in the MSM, MoO₃-SnO₂ multilayers with the highest valence
4 state of Mo and Sn elements were also assembled (Supplementary Table 2 and
5 Supplementary Fig. 11). As expected, there is no amorphous interface between MoO₃
6 and SnO₂ layers. And thus, the MoO₃/SnO₂/MoO₃ sandwiched electrode has a lower
7 ICE of 77% and a charge capacity retention of 61.4 % after 50 cycles, which is close
8 to the pure SnO₂ and much inferior to those of the MSM electrode.

9 **2.3 Theoretical calculations to understand O distribution-boosted reaction** 10 **kinetics**

11 Density functional theory (DFT) calculations were performed to understand the
12 interfacial structure in MSM. Crystal structures of SnO₂ and Mo as well as SnO₂/Mo
13 hetero-interface viewed along [001] direction are shown in Fig. 4e and Supplementary
14 Fig. 11. Three models based on the contact types are established for calculating the
15 interfacial formation energy, and model 2 shows the lowest value of -0.367 eV Å⁻²,
16 demonstrating the most stable interface state (Supplementary Table 3). According to
17 the calculated Bader charge (Supplementary Table 4), the distribution of valence
18 states at the hetero-interface for Sn and Mo are plotted in Fig. 4f. The presence of
19 SnO, MoO₂ and MoO₃ with Bader charge in range of 2.8-4.5 eV, theoretically
20 confirms the obvious interdiffusion process of O at the hetero-structure.

21 For the MSM electrode, due to the inactive Mo layer toward Li storage, the

1 redistribution of O is vitally important for Li^+ successfully passing through the Mo
2 layer to SnO_2 layer. As illustrated in detail in Fig. 4g, in the hetero-interface region, O
3 from SnO_2 diffuses into the Mo layers through the interfaces and the gaps between the
4 columnar crystals, thus, O aggregates at the SnO_2/Mo interfaces and the grain
5 boundaries of Mo. A gradient distribution of O content appears in the Mo layers, that
6 is, it gradually increases from the outside to the interface (Fig. 4g1). The
7 redistribution of O results in the loss of O to generate SnO_x ($1 < x < 2$) for the SnO_2 at
8 the interfaces, and the capturing of O to generate MoO_x ($4 < x < 6$) for Mo at the
9 interfaces and the boundaries of columnar crystals, thus forming amorphous interfaces
10 composed of SnO_x and MoO_x , and the gradient distribution of active MoO_x in Mo
11 layers toward Li storage (Fig. 4g2). Therefore, as displayed in Fig. 4g3, owing to the
12 driving force of the concentration difference of O, Li^+ can diffuse into the MSM
13 easily through the favorable pathway provided by the active MoO_x which surrounds
14 the metal Mo with good electronic conductivity. Moreover, the presence of SnO_x with
15 numerous O_{vac} in the SnO_2 layer could contribute to improved electrical conductivity
16 and reversibility of conversion reaction, leading to high ICE.^{18, 51}

17 Changes in the internal structural characteristics inevitably affect the charge
18 transfer behaviors of MSM. The in-situ formed heterojunctions formed by the metal
19 oxide semiconductors could induce a built-in electric field (E) between the interface
20 and SnO_2 layer. The calculated electrostatic potential for SnO_2 , SnO , MoO_2 and MoO_3
21 at the interface are shown in Fig. 5a. Since the work function (W_f) of the SnO_2 (7.36
22 eV) is larger than that of all other oxides, electrons transfer from the interface (SnO ,

1 MoO₃ and MoO₂) to SnO₂ across the heterojunctions.^{52, 53} Therefore, the E is
2 generated within MSM, pointing from the interface to SnO₂ layer.^{42, 54} Under the E ,
3 the barrier for the diffusion of Li⁺ in the bulk of SnO₂ also changes accordingly (Fig.
4 5b, c). Along the direction of E (A→B→C), the diffusion barrier decreases from 0.16
5 eV to 0.13 eV(A→B) and 0.08 eV to 0.05 eV(B→C), which is beneficial for the
6 insertion of Li⁺ and the inflow of electrons in MSM. The electrons/ions transfer
7 pathway and detailed mechanism of boosted charge transfer in MSM are illustrated in
8 Fig. 5d. When the battery is discharged (lithiation), an additional junction barrier
9 electric force, pointing to SnO₂ from the interface, facilitates the rapid insertion of Li⁺,
10 and this effect is strongest near the interface.^{54, 55} As clearly revealed by in-situ TEM
11 observation shown in Supplementary Video 1, the process of Li⁺ quickly passing
12 through the outer Mo layer to the SnO₂ layer has been found. After full lithiation, the
13 Li_xSn, Mo and Li₂O products from SnO_x and MoO_x lead to a Li⁺ rich region in the
14 micro-domain of SnO₂ layer and a Li⁺ poor region at the interface. Thus, a new E
15 builds with a direction from SnO₂ layer to the interface, promoting the following Li⁺
16 extraction process. These theoretical calculations offer a thorough insight into the
17 interfacial effects of electrode materials for LIBs. Due to the charge transfer driving
18 force originating from the hetero-interface, MSM electrode exhibits high-rate
19 capability and low resistance toward Li⁺ insertion and extraction, as displayed in Fig.
20 2a.

1 **2.4 In/ex-situ characterizations to reveal the interfacial effect on highly**
2 **reversible and stable conversion reactions**

3 Another important aspect that needs to be understood is how the SnO₂/Mo
4 interfaces contributed to the additional reversible capacity and highly reversible and
5 stable conversion reactions in MSM electrode. From the in-situ XRD analysis for the
6 SnO₂ electrode, as shown in Fig. 6a, the gradually disappearing of SnO₂ and
7 appearing of Sn in conversion reaction and then appearing of Li_xSn phases during
8 alloying reactions happened along with the discharge from 3.0 V to 0.01 V. However,
9 the clearly observed diffraction peak of Sn as recharged to 3 V indicates poor
10 reversibility of the conversion reaction. For the MSM multilayers in the initial cycle,
11 as shown in Fig. 6b, the Sn and Li_xSn phases which generated in the conversion and
12 alloying reactions are basically undetectable, suggesting their ultrafine grain size
13 which homogenously dispersed within the Li₂O, which leads to the largely reversible
14 conversion between SnO₂ and Sn/Li₂O in the repeated cycles in MSM. Besides, the
15 diffraction of Mo weakens and shifts to lower 2θ values when discharging, and
16 increases and shifts to the original 2θ values when charging. Obviously, the variation
17 of Mo peak throughout the cycle in MSM is much more obvious than that in the pure
18 Mo (Supplementary Fig. 13), and agrees with the GI-XRD results as the interfacial
19 density increases (Fig. 3b). Therefore, the variation of Mo peak can be used to track
20 the evolution of the interfaces, and the interfaces should expand during the Li⁺
21 insertion process and partially recover during the Li⁺ extraction process, indicating the
22 interfacial Li storage characteristic. Further tracking of the Mo peak in the subsequent

1 cycles (Fig. 6c, d) demonstrates that the interface remains stable after the 10th cycle.

2 The variation of the SnO₂/Mo interfaces in MSM has also been directly revealed
3 by in-situ TEM observation (Supplementary Video 1). As shown in Fig. 6e, f, and
4 Supplementary Figs. 14 and 15, the interface zone becomes wider and more distinct
5 during the initial 10 cycles and then reaches its steady state. Therefore, the variation
6 of the SnO₂/Mo interfaces observed by in-situ XRD and in-situ TEM demonstrates the
7 interfacial Li storage characteristic, which could be the absorption of Li at the
8 interfaces that contributes to the extra storage capacity in the MSM electrodes.^{56, 57}
9 The contribution of interfacial storage can be further enhanced by increasing the
10 interfacial density in the MSM-A and MSM-B multilayers. However, as the Mo and
11 SnO₂ layers become much thinner (such as MSM-C, D) and the interfacial density is
12 too high, the Li adsorption energy should be enhanced due to the ultra-high interfacial
13 effect.^{58, 59} It has been previously revealed that the interfacial Li adsorption helps to
14 increase the additional storage capacity in Li₂S/graphene composites before the
15 amount of adsorbed Li atoms reaches 2.⁵⁸ The high Li adsorption energy should
16 hinder the Li⁺ diffusion process, and the adsorbed Li at the interfaces is difficult to
17 detach during the delithiation process, leading to the increased irreversible capacity
18 and decreased ICE (Supplementary Fig. 16). Besides, more oxygen in SnO₂ should
19 redistribute to Mo in the multilayers with higher interfacial density, finally forming
20 MoO_x and SnO_x multilayers rather than original metal/semiconductor heterogeneous
21 interfaces. In this case, the driving force from concentration difference of O for fast
22 ion diffusion and the internal interfacial charge redistribution should be weakened,

1 resulting in inferior reversibility and stability of lithiation and delithiation reactions.
2 In contrast, in the SnO₂ or MS electrodes without or just with limited SnO₂/Mo
3 interface, poor structural stability and instantaneous collapse of active layer during
4 lithiation can be also found by in the in-situ TEM observation (Supplementary Video
5 2). These further consolidate that the Li storage behaviors at the SnO₂/Mo interfaces
6 are responsible for the relationship between the capacity increase and interfacial
7 density, as displayed in Fig. 1d.

8 To investigate the interfacial effect on the promotion of highly reversible Li
9 storage, the composition distribution of Li in the depth direction (perpendicularly to
10 the current collector) in the MSM during the 1st cycle was investigated by
11 time-of-flight secondary ion mass spectrometry (TOF-SIMS),⁶⁰ as displayed in Fig.
12 6g and Supplementary Fig. 17. The depth profiles of Li as discharged to 0.01 V,
13 charged to 1V and 3V (Fig. 6g), indicate that a large and almost equal amount of Li
14 can be released during the processes of dealloying and reverse conversion reactions,
15 meeting well with the theoretical capacity proportion of these two reactions (771
16 vs.784 mA h g⁻¹), demonstrating the fully reversible reactions in the MSM.

17 It is noted that XRD and TEM are hard to clarify the existence of Li₂O and the
18 regenerated SnO₂ which are usually amorphous. Thus, spectrum methods were
19 conducted to characterize the reversible conversion between Li₂O and SnO₂. Since
20 Li₂O turns into Li₂CO₃ when exposed to air, the variation of Li₂CO₃ could evaluate
21 the variation of Li₂O in the electrodes. As shown in Fig. 6h, the Fourier transform
22 infrared spectrometer (FTIR) spectra of the MSM electrode clearly reveal the

1 generation and disappearance of Li_2O during the discharge/charge reactions. Li_2O
2 starts to generate when discharged to 0.6 V and its content reaches the maximum at
3 0.01 V, indicating the completed conversion reaction. On the contrary, during the
4 charging process, Li_2O gradually diminishes and then disappears at 2 V, indicating
5 that Li_2O is completely reacted with Sn again and converted to SnO_2 . The regenerated
6 SnO_2 is further proven by surface-enhanced Raman spectrum (SERS) collected from
7 the MSM electrode as shown in Supplementary Fig. 18. These fully confirm that the
8 reversibility and stability of the conversion reaction in SnO_2 is greatly promoted in the
9 MSM electrode with amorphous interfaces caused by O redistribution, which is
10 responsible for the demonstrated high round-trip efficiency, increased capacity and
11 superior cycling stability in the SnO_2 -Mo multilayers.

12 **3 Conclusions**

13 To summarize, we assembled the SnO_2 -Mo multilayers with adjustable interfaces
14 and tunable oxygen distribution, and established a model to quantify the regulating
15 effect of SnO_2 /Mo interfaces on the stability and reversibility of conversion between
16 SnO_2 and Sn/ Li_2O . Benefiting from the multifaceted interfacial effects on the
17 structural stability, Li storage capacity and reaction kinetics, Mo/ SnO_2 /Mo exhibits
18 good cycling stability and accelerated charge-transfer kinetics, realizing a
19 breakthrough performance with high average ICE of 92.6 % and large capacity of
20 1067 mA h g^{-1} remained 100 % after 200 cycles. Furthermore, we clarified that the
21 redistribution of oxygen between SnO_2 and Mo layers helps to form SnO_2 /Mo

1 amorphous interfaces, thereby providing additional reversible capacity and promoting
2 the highly reversible and rapid conversion reaction in lithiated SnO₂. This work based
3 on interface engineering and modulation of oxygen distribution provides a novel
4 fundamental strategy to design highly reversible and stable conversion-type electrode
5 materials for large capacity Li storage.

6 **4 Experimental**

7 **4.1 Preparation of multilayer thin film electrodes**

8 All multilayer thin film electrodes were deposited on Cu foil substrates (6*6
9 cm²) using a KYKY JGB-560 magnetron sputtering system. The targets of SnO₂, Mo
10 and MoO₃ have a diameter of 60 mm and a thickness of 5 mm. Under optimized
11 conditions, in a typical deposition, a radio frequency magnetron (power 120 W, 2.0 Pa
12 Ar as the working gas) was used during deposition after a base pressure of 1.0 *10⁻⁴
13 Pa was achieved. The various multilayer thin films, namely, SnO₂, SnO₂-Mo and
14 SnO₂-MoO₃, were comparatively investigated as anodes for LIBs.

15 To prepare the sample for surface enhanced Raman spectroscopy (SERS)
16 measurement, colloid of Au nanoparticles was deposited on the surface of the SnO₂
17 and Mo/SnO₂/Mo electrodes.

18 **4.2 Materials characterization**

19 X-ray diffraction (XRD) was performed with a PANalytical X'Pert Pro Alpha-1
20 diffractometer using Cu K α radiation. The microstructure was characterized using a

1 Carl Zeiss Supra 40 field emission scanning electron microscope (SEM) and a
2 high-resolution transmission electron microscope (TEM, JEOL JEM-2100F)
3 operating at 200 kV. The compositions of the layers were determined with an
4 energy-dispersive spectrometer (EDS) attached to the TEM. X-ray photoelectron
5 spectroscopy (XPS) was performed with a PerkinElmer PHI 5000c XPS system using
6 the C 1s peak at 284.8 eV as a reference. TOF-SIMS measurements were conducted
7 on a TOF-SIMS spectrometer (TESCAN GAIA3 model 2016 UHR SEM). The
8 TOF-SIMS measurements were conducted in positive mode. A pulsed 30 keV Ga⁺ ion
9 beam was used in the high current mode for depth profiling. The SERS measurement
10 was conducted with a laser Raman spectrometer (Raman, Horiba) at an excitation
11 wavelength of 532.0 nm. The accurate component analysis was conducted by an
12 Escabe 250 X-ray photoelectron spectrometer (Thermo Fisher Scientific, USA).
13 FTIR spectra were obtained by a Nicolet iS50FTIR spectroscopy, equipped with
14 attenuated total reflectance technique. The measurement worked in the range of
15 4000-700 cm⁻¹.

16 For the ex-situ measurement of electrochemically tested electrodes, the samples
17 were carefully stored and transferred to minimize air exposure. The reacted film
18 electrodes at different states were prepared by discharging/charging to a controlled
19 cutoff voltage. These electrodes were removed from the electrochemical cells, rinsed
20 with DMC and dried under vacuum in the ante-chamber of an argon filled glove box.

1 **4.3 In-Situ Examinations**

2 In-situ XRD analysis was conducted with a PANalytical X'Pert Pro Alpha-1
3 diffractometer using Cu Ka radiation and investigated by a homemade cell that was
4 sealed by Be foil as the X-ray penetrator, accompanied with the lithiation/delithiation
5 process. The 2θ range of each scan started from 25° to 45° with step increment of 0.02°
6 at step size of 0.26° . In-situ TEM measurement was performed on a JEOL 1400 TEM.
7 The MSM electrode was displayed on an Au rod as the working electrode, while a
8 small film of Li metal was scratched on a W wire as the counter electrode. A thin layer
9 of Li_2O was expected to form as the solid electrolyte during the charge transfer
10 process. When physical contact between the two electrodes was encountered, a
11 potential bias of ± 3 V versus Li/Li^+ was applied to drive the diffusion of Li^+ .

12 **4.4 Electrochemical measurements**

13 CR2016 coin-type half-cells were assembled in a glove box with Li metal foil as
14 the counter electrode and a polyethylene membrane as the separator. The electrolyte
15 was a solution of 1 M LiPF_6 in a mixture of ethylene carbonate (EC) and diethyl
16 carbonate (DEC) with a volume ratio of 1:2, and 10 wt% fluoroethylene carbonate
17 (FEC) was added. The electrochemical performance of the different film electrodes
18 was measured by galvanostatic charge–discharge cycling using a multi-channel
19 battery test system (LAND CT2001A) at various current densities, and cutoff
20 potentials of 0.01 V for discharging and 3.0 V or 1.0 V for charging.

1 4.5 Computational Method

2 Our SnO₂/Mo heterostructure models consist of a slab of Mo deposited on top of
3 a SnO₂ surface. According to previous reports, the (110) surface of rutile SnO₂ (space
4 group P4₂/mnm) is the most stable, so we selected the (110) surface of SnO₂ to
5 match with the (110) surface of cubic Mo (space group $Im\bar{3}m$).

6 All calculations were performed by using the projector augmented wave (PAW)
7 method within density functional theory (DFT) as implemented in the Vienna ab initio
8 simulation package (VASP).^{24, 61} Generalized gradient approximation (GGA)
9 parameterized by Perdew-Burke-Ernzerhof (PBE) formula was employed for
10 evaluating the electron exchange correlation energy. The DFT-D3 method of Grimme
11 was used to describe the weak dispersion forces.⁶² The energy cutoff for the plane
12 waves was set to 500 eV. Brillouin-zone integrations were approximated by using
13 special k -point sampling of Monkhorst-Park scheme [MP76] with a k -point mesh
14 resolution of $2\pi \times 0.03 \text{ \AA}^{-1}$. The structural parameters were fully optimized until the
15 energy on each atom was less than 10^{-5} eV and the forces on each atom were less than
16 0.01 eV/\AA . The *ab initio* molecular dynamics (AIMD) simulations were performed in
17 supercell models and only the gamma point was used for the Brillouin zone sampling
18 to keep the computational cost at a reasonable level. The time step was set to 2fs. The
19 NVT ensemble using Nosé-Hoover thermostat was adopted. For Li⁺ diffusion into the
20 SnO₂ surface, the climbing image nudged elastic band (CI-NEB) method was used in
21 supercell models.⁶³

1 **Acknowledgements**

2 This work was supported by the National Natural Science Foundation of China (grant
3 numbers: 51822104, 52071144, and 51621001).

4 **Author contributions**

5 R.H., M.Z. and X.L. conceived the idea and designed the experiments. X.L., H.Z.,
6 L.T. and X.X. conducted the material preparation, electrochemical measurements and
7 materials characterization. X.L. performed the ex-situ measurements and the data
8 analysis. X.L., J.C. and X.Y. performed in-situ experiments and participated in data
9 analysis. X.Z. and S.W. performed the theoretical calculations. X.L., J.C. and J.H.
10 wrote the paper with assistance from coauthors.

11 **Competing interests**

12 The authors declare no competing interests.

13

1 **References**

- 2 1. Sun, Y., Liu, N. & Cui, Y. Promises and challenges of nanomaterials for
3 lithium-based rechargeable batteries. *Nat. Energy*. **1**, 16071 (2016).
- 4 2. Gur, T. M. Review of electrical energy storage technologies, materials and
5 systems: challenges and prospects for large-scale grid storage. *Energy Environ. Sci.*
6 **11**, 2696-2767 (2018).
- 7 3. Li, M., Lu, J., Chen, Z. & Amine, K. 30 Years of Lithium-Ion Batteries. *Adv.*
8 *Mater.* **30**, 18800561 (2018).
- 9 4. Obrovac, M. N. & Chevrier, V. L. Alloy Negative Electrodes for Li-Ion Batteries.
10 *Chem. Rev.* **114**, 11444-11502 (2014).
- 11 5. Reddy, M. V., Rao, G. V. S. & Chowdari, B. V. R. Metal Oxides and Oxysalts as
12 Anode Materials for Li Ion Batteries. *Chem. Rev.* **113**, 5364-5457 (2013).
- 13 6. Retoux, R., Brousse, T. & Schleich, D. M. High-resolution electron microscopy
14 investigation of capacity fade in SnO₂ electrodes for lithium-ion batteries. *J.*
15 *Electrochem. Soc.* **146**, 2472-2476 (1999).
- 16 7. Song, M. J., Kim, I. T., Kim, Y. B. & Shin, M. W. Self-standing, binder-free
17 electrospun Co₃O₄/carbon nanofiber composites for non-aqueous Li-air batteries.
18 *Electrochim. Acta.* **182**, 289-296 (2015).
- 19 8. Hu, R. Z., Sun, W., Liu, H., Zeng, M. Q. & Zhu, M. The fast filling of nano-SnO₂
20 in CNTs by vacuum absorption: a new approach to realize cyclic durable anodes
21 for lithium ion batteries. *Nanoscale*. **5**, 11971-11979 (2013).
- 22 9. Idota, Y., Kubota, T., Matsufuji, A., Maekawa, Y. & Miyasaka, T. Tin-based

- 1 amorphous oxide: A high-capacity lithium-ion-storage material. *Science*. **276**,
2 1395-1397 (1997).
- 3 10. Ji, G., Ma, Y. & Lee, J. Y. Mitigating the initial capacity loss (ICL) problem in
4 high-capacity lithium ion battery anode materials. *J. Mater. Chem.* **21**, 9819-9824
5 (2011).
- 6 11. Cabana, J., Monconduit, L., Larcher, D. & Rosa Palacin, M. Beyond
7 Intercalation-Based Li-Ion Batteries: The State of the Art and Challenges of
8 Electrode Materials Reacting Through Conversion Reactions. *Adv. Mater.* **22**,
9 E170-E192 (2010).
- 10 12. Huang, J. Y. et al. In Situ Observation of the Electrochemical Lithiation of a
11 Single SnO₂ Nanowire Electrode. *Science*. **330**, 1515-1520 (2010).
- 12 13. Poizot, P., Laruelle, S., Grugeon, S., Dupont, L. & Tarascon, J.-M. Nano-Sized
13 Transition-Metal Oxides as Negative-Electrode Materials for Lithium-Ion
14 Batteries. *Nature*. **407**, 496-499 (2000).
- 15 14. Hu, R. et al. Dramatically enhanced reversibility of Li₂O in SnO₂-based electrodes:
16 the effect of nanostructure on high initial reversible capacity. *Energy Environ. Sci.*
17 **9**, 595-603 (2016).
- 18 15. Hu, R. et al. Inhibiting Sn coarsening to enhance the reversibility of conversion
19 reaction in lithiated SnO₂ anodes by application of super-elastic NiTi films. *Acta*
20 *Mater.* **109**, 248-258 (2016).
- 21 16. Hu, R. et al. Stabilizing the Nanostructure of SnO₂ Anodes by Transition Metals:
22 A Route to Achieve High Initial Coulombic Efficiency and Stable Capacities for

- 1 Lithium Storage. *Adv. Mater.* **29**, 1605006 (2017).
- 2 17. Meduri, P., Clark, E., Dayalan, E., Sumanasekera, G. U. & Sunkara, M. K.
3 Kinetically limited de-lithiation behavior of nanoscale tin-covered tin oxide
4 nanowires. *Energy Environ. Sci.* **4**, 1695-1699 (2011).
- 5 18. Hu, R. et al. Inhibiting grain coarsening and inducing oxygen vacancies: the roles
6 of Mn in achieving a highly reversible conversion reaction and a long life
7 SnO₂-Mn-graphite ternary anode. *Energy Environ. Sci.* **10**, 2017-2029 (2017).
- 8 19. Ma, Y. et al. Conversion/alloying lithium-ion anodes - enhancing the energy
9 density by transition metal doping. *Sustain. Energy Fuels.* **2**, 2601-2608 (2018).
- 10 20. Meng, T., Qin, J. W., Yang, Z., Zheng, L. R. & Cao, M. H. Significantly improved
11 Li-ion diffusion kinetics and reversibility of Li₂O in a MoO₂ anode: the effects of
12 oxygen vacancy-induced local charge distribution and metal catalysis on lithium
13 storage. *J. Mater. Chem. A.* **7**, 17570-17580 (2019).
- 14 21. Ma, D. T., Li, Y. L., Zhang, P. X. & Lin, Z. Q. Oxygen Vacancy Engineering in
15 Tin(IV) Oxide Based Anode Materials toward Advanced Sodium-Ion Batteries.
16 *Chemsuschem.* **11**, 3693-3703 (2018).
- 17 22. Zheng, Y. et al. Atomic Interface Engineering and Electric-Field Effect in
18 Ultrathin Bi₂MoO₆ Nanosheets for Superior Lithium Ion Storage. *Adv. Mater.* **29**,
19 1700396 (2017).
- 20 23. Peng, B. et al. Ultrafast charge transfer in MoS₂/WSe₂ p-n Heterojunction. *2D*
21 *Mater.* **3**, 02050 (2016).
- 22 24. Jariwala, D., Marks, T. J. & Hersam, M. C. Mixed-dimensional van der Waals

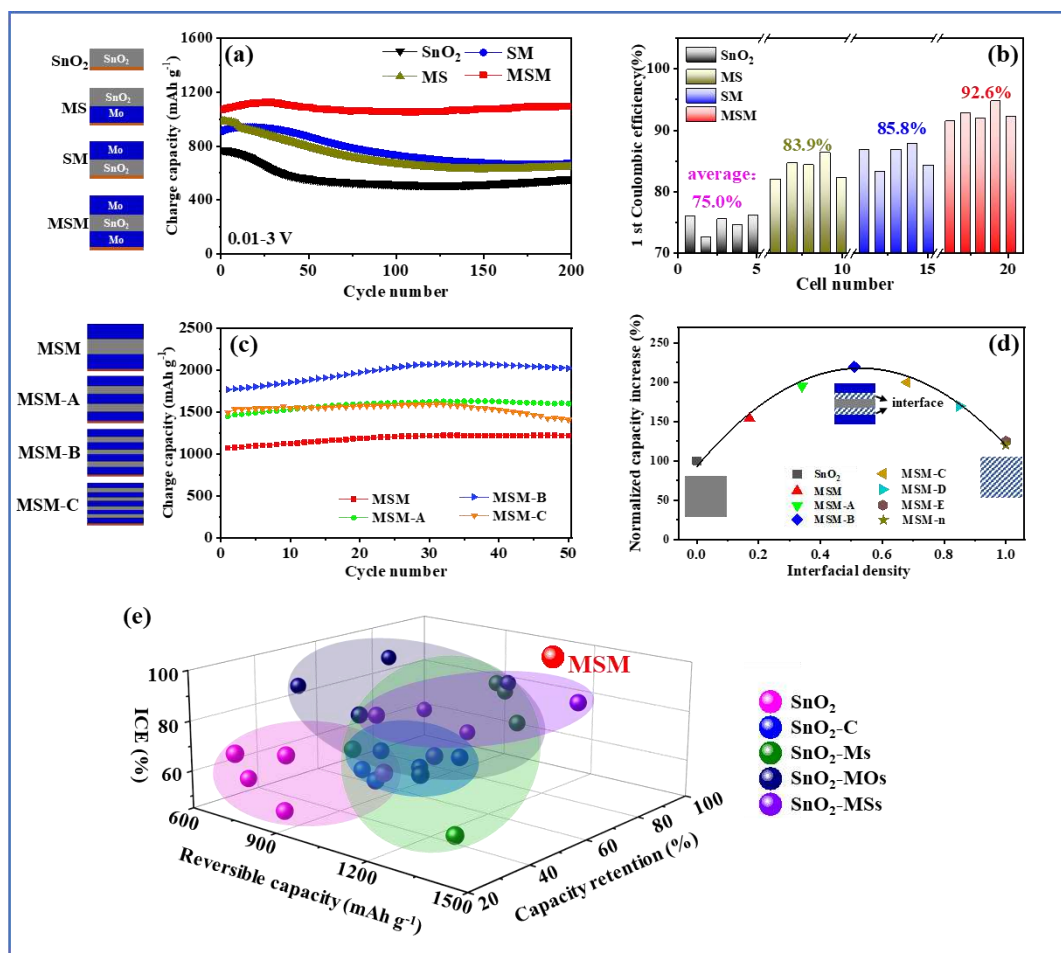
- 1 heterostructures. *Nat. Mater.* **16**, 170-181 (2017).
- 2 25. Hu, R. et al. Unveiling critical size of coarsened Sn nanograins for achieving high
3 round-trip efficiency of reversible conversion reaction in lithiated SnO₂
4 nanocrystals. *Nano Energy.* **45**, 255-265 (2018).
- 5 26. Jiang, Y., Yuan, T., Yan, M. & Sun, W. Electrostatic spray deposition of porous
6 SnO/graphene anode films and their enhanced lithium-storage properties. *ACS*
7 *Appl. Mater. Interfaces.* **4**, 6216-6220 (2012).
- 8 27. Cheng, Y. Y. et al. Adjusting the Chemical Bonding of SnO₂@CNT Composite for
9 Enhanced Conversion Reaction Kinetics. *Small.* **13**, 1700656 (2017).
- 10 28. Jin, Y. H., Min, K. M., Seo, S. D., Shim, H. W. & Kim, D. W. Enhanced Li
11 Storage Capacity in 3 nm Diameter SnO₂ Nanocrystals Firmly Anchored on
12 Multiwalled Carbon Nanotubes. *J. Phys. Chem. A.* **115**, 22062-22067 (2011).
- 13 29. Paek, S. M., Yoo, E. & Honma, I. Enhanced Cyclic Performance and Lithium
14 Storage Capacity of SnO₂/Graphene Nanoporous Electrodes with
15 Three-Dimensionally Delaminated Flexible Structure. *Nano Lett.* **9**, 72-75 (2009).
- 16 30. Xu, W. W. et al. Hierarchical Graphene-Encapsulated Hollow SnO₂@SnS₂
17 Nanostructures with Enhanced Lithium Storage Capability. *ACS Appl. Mater.*
18 *Interfaces.* **7**, 22533-22541 (2015).
- 19 31. Yang, L. Y. et al. Hollow bean-pod-like SiO₂-supported- SnO₂/C nanocomposites
20 for durable lithium and sodium storage. *J. Mater. Chem. A.* **5**, 1629-1636 (2017).
- 21 32. Chen, Y. L. et al. Ultrafine Mo-doped SnO₂ nanostructure and derivative
22 Mo-doped Sn/C nanofibers for high-performance lithium-ion batteries. *Nanoscale.*

- 1 **10**, 17378-17387 (2018).
- 2 33. He, Q. et al. Solvent-Free Synthesis of Uniform MOF Shell-Derived Carbon
3 Confined SnO₂/Co Nanocubes for Highly Reversible Lithium Storage. *Small*. **13**,
4 (2017).
- 5 34. Li, Z. F. et al. Facile Preparation of Graphene/SnO₂ Xerogel Hybrids as the Anode
6 Material in Li-Ion Batteries. *ACS Appl. Mater. Interfaces*. **7**, 27087-27095 (2015).
- 7 35. Ma, C. R. et al. Carbon coated SnO₂ nanoparticles anchored on CNT as a superior
8 anode material for lithium-ion batteries. *Nanoscale*. **8**, 4121-4126 (2016).
- 9 36. Tian, Q., Tian, Y., Zhang, Z., Yang, L. & Hirano, S.-i. Double-shelled support and
10 confined void strategy to improve the lithium storage properties of SnO₂/C anode
11 materials for lithium-ion batteries. *J. Mater. Chem. A*. **3**, 18036-18044 (2015).
- 12 37. Choi, J., Kim, W. S. & Hong, S. H. Highly stable SnO₂-Fe₂O₃-C hollow spheres
13 for reversible lithium storage with extremely long cycle life. *Nanoscale*. **10**,
14 4370-4376 (2018).
- 15 38. Guo, W. B. et al. SnO₂@C@VO₂ Composite Hollow Nanospheres as an Anode
16 Material for Lithium-Ion Batteries. *ACS Appl. Mater. Interfaces*. **10**, 14993-15000
17 (2018).
- 18 39. Liang, T. et al. A scalable ternary SnO₂-Co-C composite as a high initial
19 coulombic efficiency, large capacity and long lifetime anode for lithium ion
20 batteries. *J. Mater. Chem. A*. **6**, 7206-7220 (2018).
- 21 40. Liu, Y. et al. Highly Conductive In- SnO₂/RGO Nano-Heterostructures with
22 Improved Lithium-Ion Battery Performance. *Sci. Rep.* **6**, (2016).

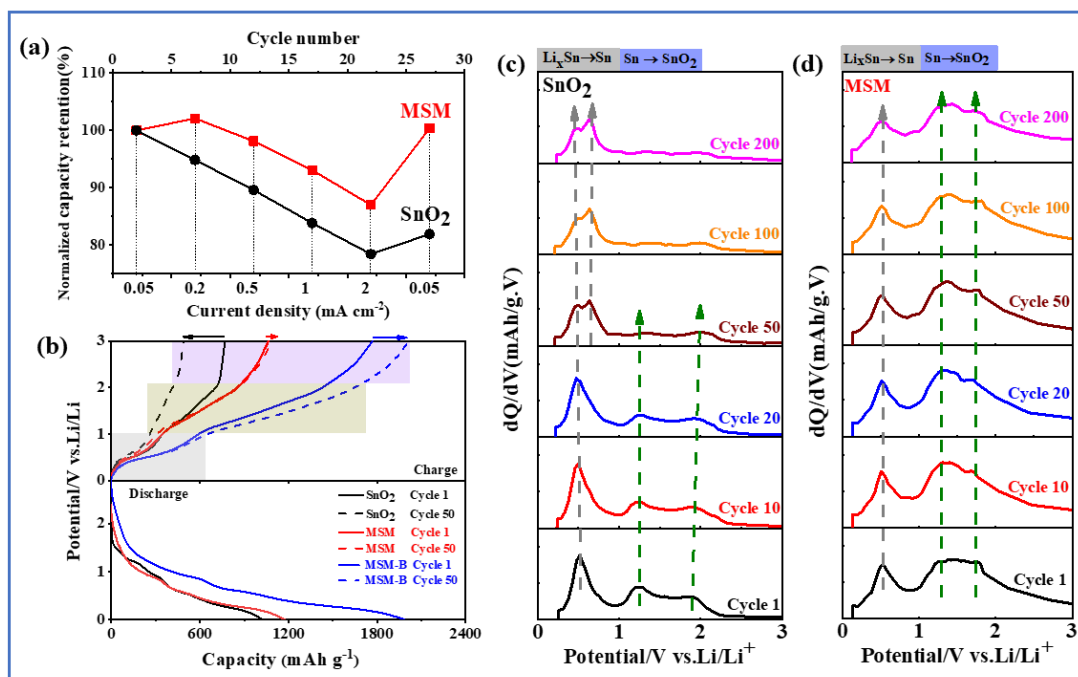
- 1 41. Zhao, P., Yue, W. B., Yuan, X. & Bao, H. Y. Exceptional lithium anodic
2 performance of Pd-doped graphene-based SnO₂ nanocomposite. *Electrochim. Acta.*
3 **225**, 322-329 (2017).
- 4 42. Chen, K. et al. A new generation of high performance anode materials with
5 semiconductor heterojunction structure of SnSe/SnO₂@Gr in lithium-ion batteries.
6 *Chem. Eng. J.* **347**, 552-562 (2018).
- 7 43. Jiang, Y. Z. et al. Ultrafast, Highly Reversible, and Cycle-Stable Lithium Storage
8 Boosted by Pseudocapacitance in Sn-Based Alloying Anodes. *Adv. Mater.* **29**,
9 1606499 (2017).
- 10 44. Li, M. et al. In situ carbon encapsulation of vertical MoS₂ arrays with SnO₂ for
11 durable high rate lithium storage: dominant pseudocapacitive behavior. *Nanoscale.*
12 **10**, 741-751 (2018).
- 13 45. Park, G. D., Lee, J. K. & Kang, Y. C. Design and synthesis of Janus-structured
14 mutually doped SnO₂-Co₃O₄ hollow nanostructures as superior anode materials
15 for lithium-ion batteries. *J. Mater. Chem. A.* **5**, 25319-25327 (2017).
- 16 46. Ye, H. J., Li, H. Q., Jiang, F. Q., Yin, J. & Zhu, H. In situ fabrication of
17 nitrogen-doped carbon-coated SnO₂/SnS heterostructures with enhanced
18 performance for lithium storage. *Electrochim. Acta.* **266**, 170-177 (2018).
- 19 47. Wang, X. et al. Mo-doped SnO₂ mesoporous hollow structured spheres as anode
20 materials for high-performance lithium ion batteries. *Nanoscale.* **7**, 3604-3613
21 (2015).
- 22 48. Kim, H.-S. et al. Oxygen vacancies enhance pseudocapacitive charge storage

- 1 properties of MoO_{3-x} . *Nat. Mater.* **16**, 454-462 (2017).
- 2 49. Zhang, G. B. et al. α - MoO_{3-x} by plasma etching with improved capacity and
3 stabilized structure for lithium storage. *Nano Energy.* **49**, 555-563 (2018).
- 4 50. Geng, Z. et al. Oxygen Vacancies in ZnO Nanosheets Enhance CO_2
5 Electrochemical Reduction to CO. *Angew. Chem. Int. Ed.* **57**, 6054-6059 (2018).
- 6 51. Dong, W. J. et al. A Robust and Conductive Black Tin Oxide Nanostructure Makes
7 Efficient Lithium-Ion Batteries Possible. *Adv. Mater.* **29**, (2017).
- 8 52. Gao, X., Shen, Y. Q., Ma, Y. Y., Wu, S. Y. & Zhou, Z. X. First-principles insights
9 into efficient band gap engineering of the blue phosphorus/g- C_3N bilayer
10 heterostructure via an external vertical strain. *Appl. Surf. Sci.* **479**, 1098-1104
11 (2019).
- 12 53. Liu, J. J. & Hua, E. D. High Photocatalytic Activity of Heptazine-Based
13 g- $\text{C}_3\text{N}_4/\text{SnS}_2$ Heterojunction and Its Origin: Insights from Hybrid DFT. *J. Phys.*
14 *Chem. A.* **121**, 25827-25835 (2017).
- 15 54. Pal, M., Tsujigami, Y., Yoshikado, A. & Sakata, H. Electrical and optical
16 properties of $\text{MoO}_3\text{-TeO}_2$ amorphous films prepared by PVD method. *Phys. stat.*
17 *sol. (a).* **182**, 727-736 (2000).
- 18 55. Feng, H. J., Paudel, T. R., Tsymbal, E. Y. & Zeng, X. C. Tunable Optical
19 Properties and Charge Separation in $\text{CH}_3\text{NH}_3\text{Sn}_x\text{Pb}_{1-x}\text{I}_3/\text{TiO}_2$ -Based Planar
20 Perovskites Cells. *J. Am. Chem. Soc.* **137**, 8227-8236 (2015).
- 21 56. Shon, J. K. et al. Discovery of abnormal lithium-storage sites in molybdenum
22 dioxide electrodes. *Nat. Commun.* **7**, (2016).

- 1 57. Fang, L. et al. Hetero-interface constructs ion reservoir to enhance conversion
2 reaction kinetics for sodium/lithium storage. *Energy Storage Materials*. **18**,
3 107-113 (2019).
- 4 58. Lv, Y. et al. Interfacial effect on the electrochemical properties of the layered
5 graphene/metal sulfide composites as anode materials for Li-ion batteries. *Surf.*
6 *Sci.* **651**, 10-15 (2016).
- 7 59. Stournara, M. E. & Shenoy, V. B. Enhanced Li capacity at high lithiation
8 potentials in graphene oxide. *J. Power Sources*. **196**, 5697-5703 (2011).
- 9 60. You, Y., Dolocan, A., Li, W. & Manthiram, A. Understanding the Air-Exposure
10 Degradation Chemistry at a Nanoscale of Layered Oxide Cathodes for
11 Sodium-Ion Batteries. *Nano Lett.* **19**, 182-188 (2019).
- 12 61. Meng, T., Hao, Y. N., Qin, J. W. & Cao, M. H. Interface-Engineering-Induced
13 Electric Field Effect and Atomic Disorder in Cobalt Selenide for High-Rate and
14 Large-Capacity Lithium Storage. *ACS Sustain. Chem. Eng.* **7**, 4657-4665 (2019).
- 15 62. Grimme, S., Antony, J., Ehrlich, S. & Krieg, H. A consistent and accurate ab initio
16 parametrization of density functional dispersion correction (DFT-D) for the 94
17 elements H-Pu. *J. Chem. Phys.* **132**, (2010).
- 18 63. Henkelman, G., Uberuaga, B. P. & Jonsson, H. A climbing image nudged elastic
19 band method for finding saddle points and minimum energy paths. *J. Chem. Phys.*
20 **113**, 9901-9904 (2000).



1
2 **Fig. 1 Highly reversible and stable Li storage properties of SnO₂-Mo electrodes in half cells.**
3 (a) Comparison of charge capacity. (b) Summary of the ICEs from every five cells for SnO₂, SM,
4 MS and MSM electrodes. (c) Cycling performance of MSM-A, MSM-B and MSM-C electrodes in
5 the initial 50 cycles. (d) The relationship between normalized capacity increase and interfacial
6 density. The charge capacity of each electrode is taken from the 5th cycle. The dotted lines
7 represent the capacity increase calculated from the fitting curves. (e) The reversible capacities,
8 capacity retentions after 200 cycles and ICEs of SnO₂-based anodes for LIBs reported in the recent
9 literatures, including the pure SnO₂,^{25, 26, 29-31} SnO₂-C,^{27, 28, 34-36} SnO₂-Metals (SnO₂-Ms),^{32, 33, 39-41}
10 SnO₂-Metal oxides (SnO₂-MOs)^{33, 37, 38, 43, 45} and SnO₂-Metal sulfides (SnO₂-MSs)^{30, 31, 42, 44, 46}.
11 The red sphere represents the average electrochemical performance of the MSM electrode.



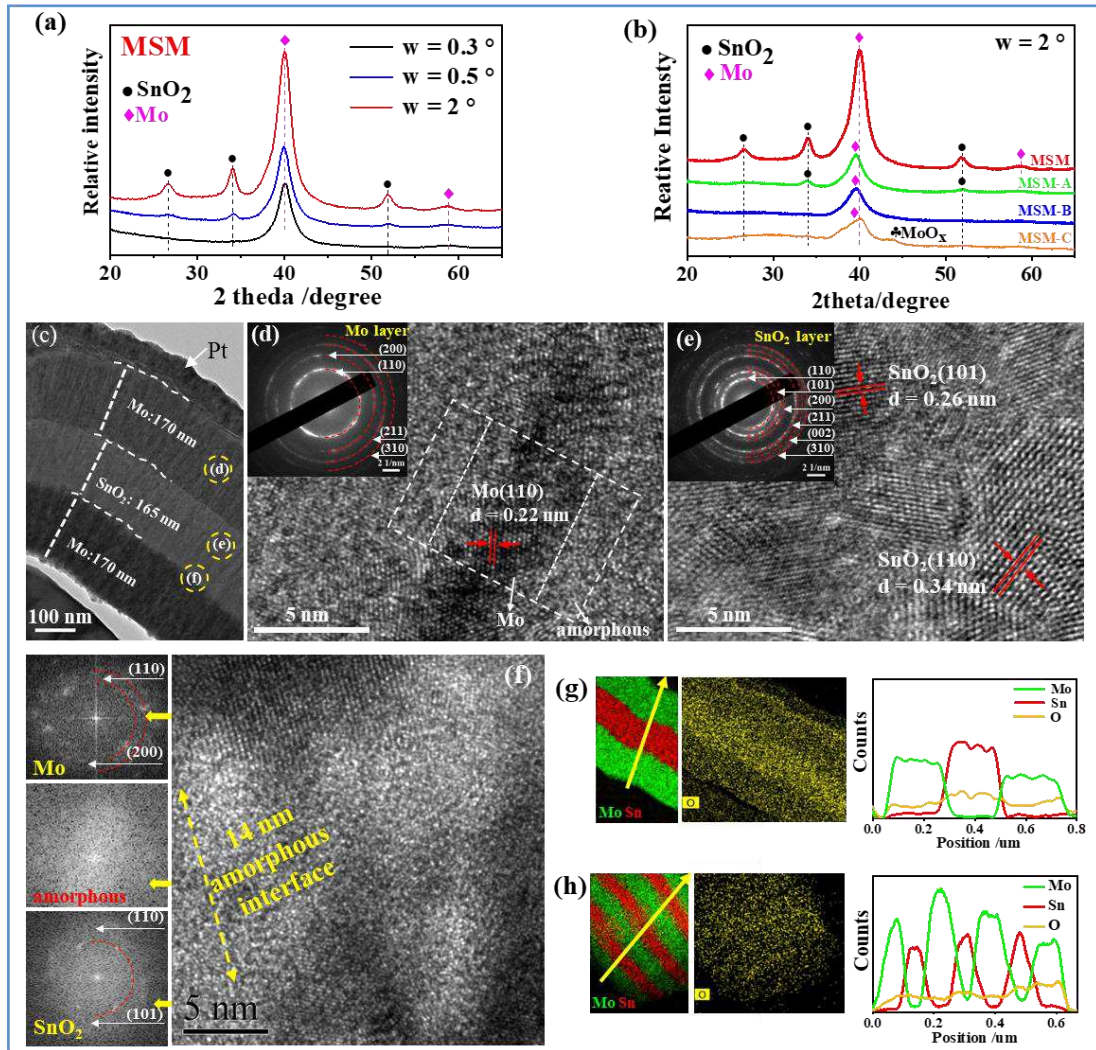
1

2 **Fig. 2 Comparison of the rate capabilities and reaction reversibility for the SnO₂ and MSM**

3 **electrodes. (a) Rate capabilities of SnO₂ and MSM electrodes. (b) Charge-discharge profiles of**

4 **SnO₂, MSM and MSM-B electrodes at the 1st and 50th cycles. (c, d) Differential charge capacity**

5 **vs. voltage curve of SnO₂ and MSM electrodes at the 1st, 10th, 20th, 50th, 100th and 200th cycles.**



1

2 **Fig. 3 GI-XRD and FIB-TEM characterizations of the structure and cross-sectional**

3 **morphology of MSM, MSM-A, MSM-B and MSM-C. (a) GI-XRD patterns of MSM with the**

4 **incident angle of 0.3°, 0.5° and 2.0°. (b) GI-XRD patterns of MSM, MSM-A, MSM-B and**

5 **MSM-C with the incident angle of 2°. (c-g) TEM observation of MSM. (c) Typical FIB-TEM**

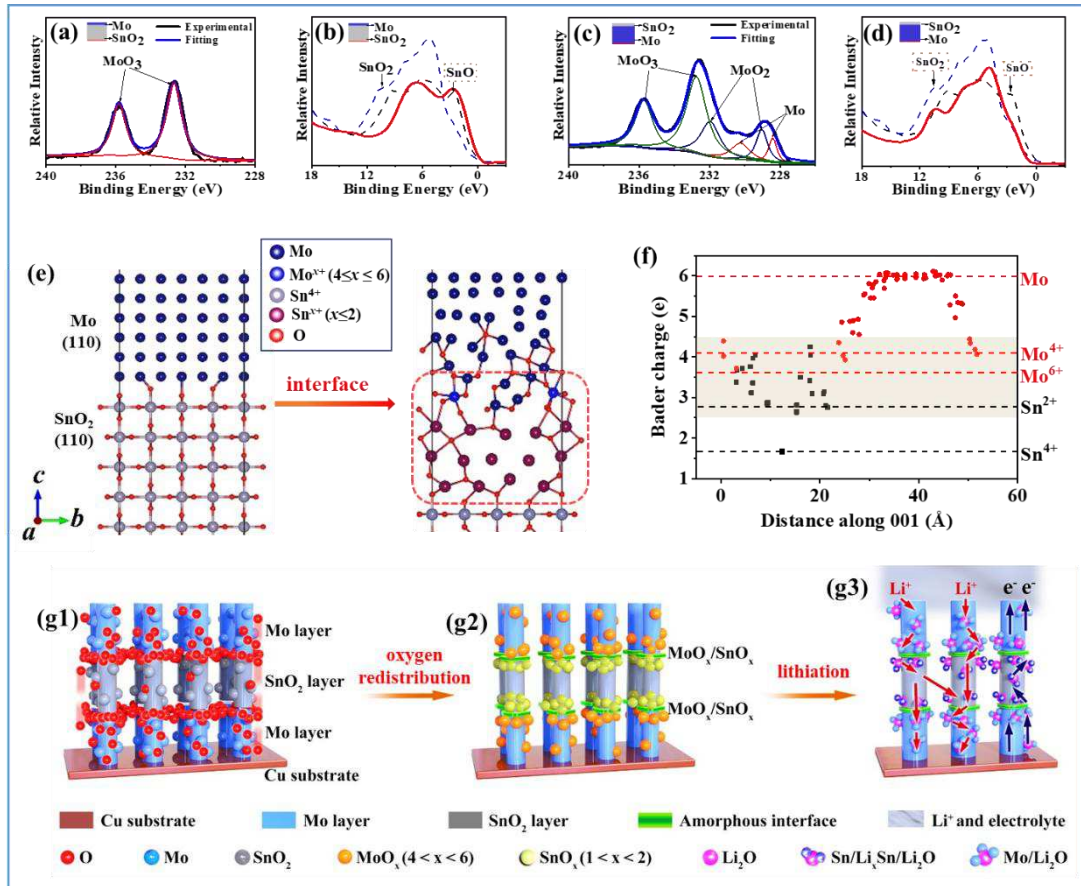
6 **image of cross-sectional morphology. (d, e) HRTEM images of the Mo and SnO₂ layers, insets in**

7 **(d) and (e) are the corresponding SAED images. (f) HRTEM image at the interface between Mo**

8 **and SnO₂ layers, and FFT images of corresponding regions. (g, h) EDS mapping and line-scan**

9 **images of Sn, Mo and O elements for MSM and MSM-B.**

10



1

2 **Fig. 4 XPS analysis and DFT calculations of valence states and charge distributions at the**

3 **interfaces of MSM. (a-d) XPS spectra at the interfaces of MSM. (a) Mo 3d at the up side of**

4 **interface in MSM. (b) Valence band Spectrum of Sn 3d at the up side of interface in MSM. (c) Mo**

5 **3d at the down side of interface in MSM. (d) Valence band Spectrum of Sn 3d at the down side of**

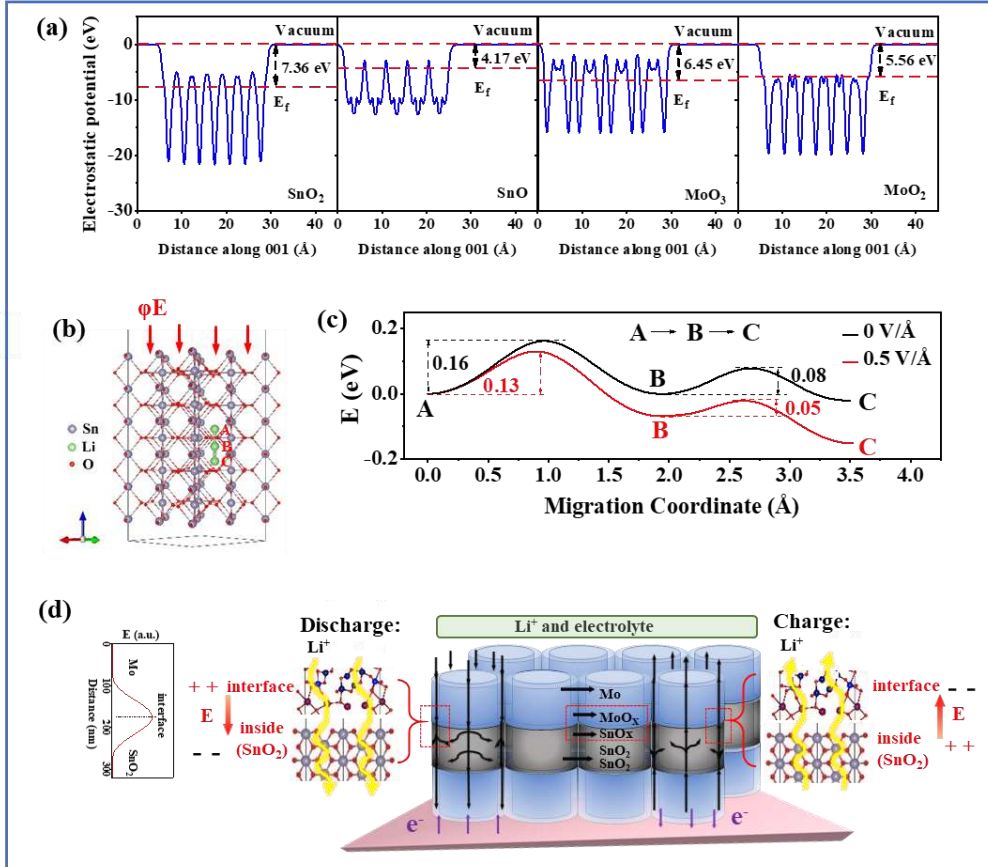
6 **interface in MSM. (e) Crystal structure of Mo, SnO₂ and the interface viewed along [001]**

7 **direction. (f) Distribution of valence states of Sn and Mo atoms at the hetero-interface in MSM. (g)**

8 **Schematic showing the redistribution of O and the rapid transfer process of electrons/ions in**

9 **MSM.**

10



1

2 **Fig. 5 DFT calculations of the Li^+ transfer dynamics boosted by induced electric field effect**

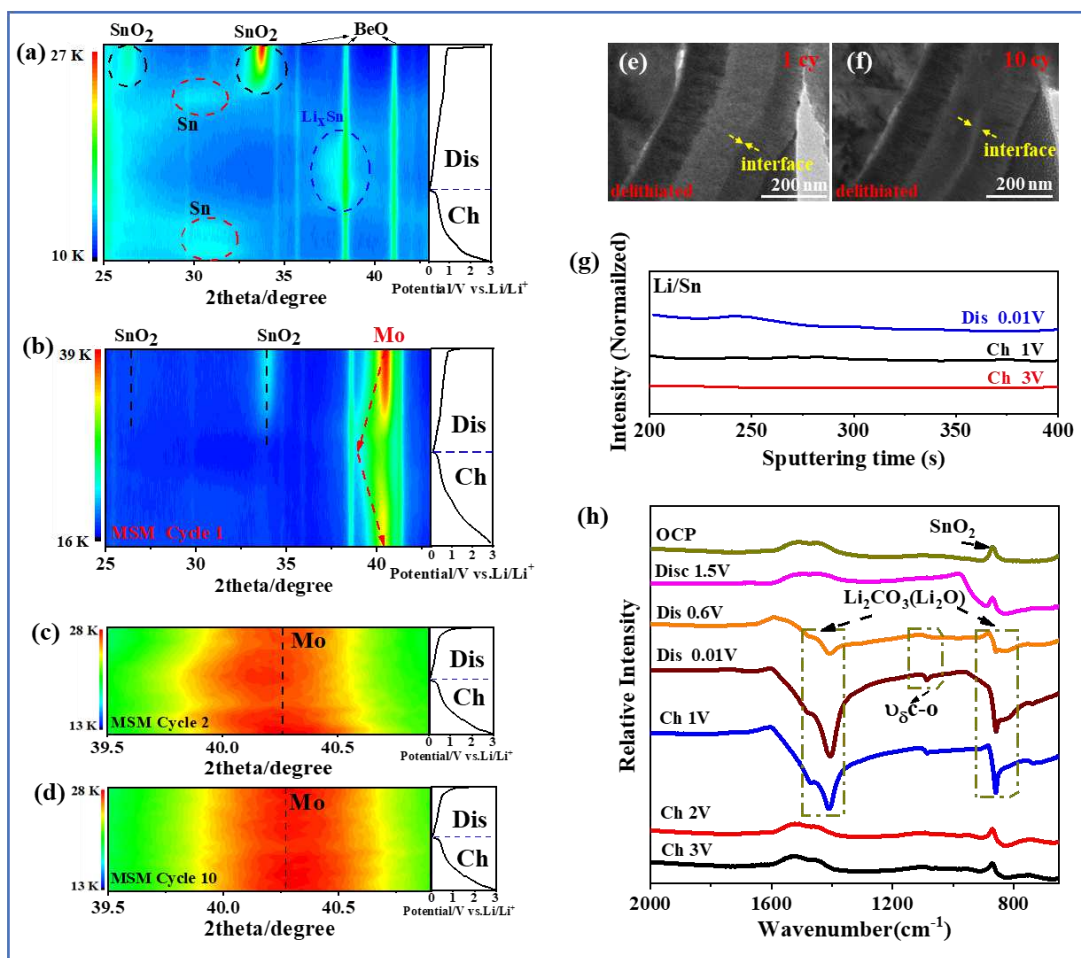
3 **(E).** (a) Calculated electrostatic potential of SnO_2 , SnO , MoO_3 , and MoO_2 , respectively. (b)

4 Crystal structure of SnO_2 with three Li^+ intercalated at A, B, and C sites. (c) Calculated diffusion

5 barrier of Li^+ from A→B and B→C along the electric field. (d) Schematic diagram of the effect of

6 E and the mechanism of boosted charge transfer within MSM.

7



1

2 **Fig. 6 In/ex-situ observations of morphology and phase evolution of MSM electrode during**

3 **lithiation/delithiation processes. (a-d) Contour plots of in-situ XRD patterns against the voltage**

4 **for the SnO₂ and MSM electrodes. (a) SnO₂ electrode during the 1st cycle. (b-d) MSM electrode**

5 **during the 1st cycle (b), 2nd cycle (c) and 10th cycle (d). (e, f) In-situ TEM observation of MSM**

6 **electrode at the fully delithiated status in the 1st cycle (e) and 10th cycle (f). (g) TOF-SIMS**

7 **characterization for Li/Sn depth profiles as discharged to 0.01 V, charged to 1V and 3V in the 1st**

8 **cycle. (h) Ex-situ FTIR spectra at seven different states during the 1st cycle, namely OCP,**

9 **discharged to 1.5V, 0.6V and 0.01 V, recharged to 1V, 2V and 3.0 V.**

10

Figures

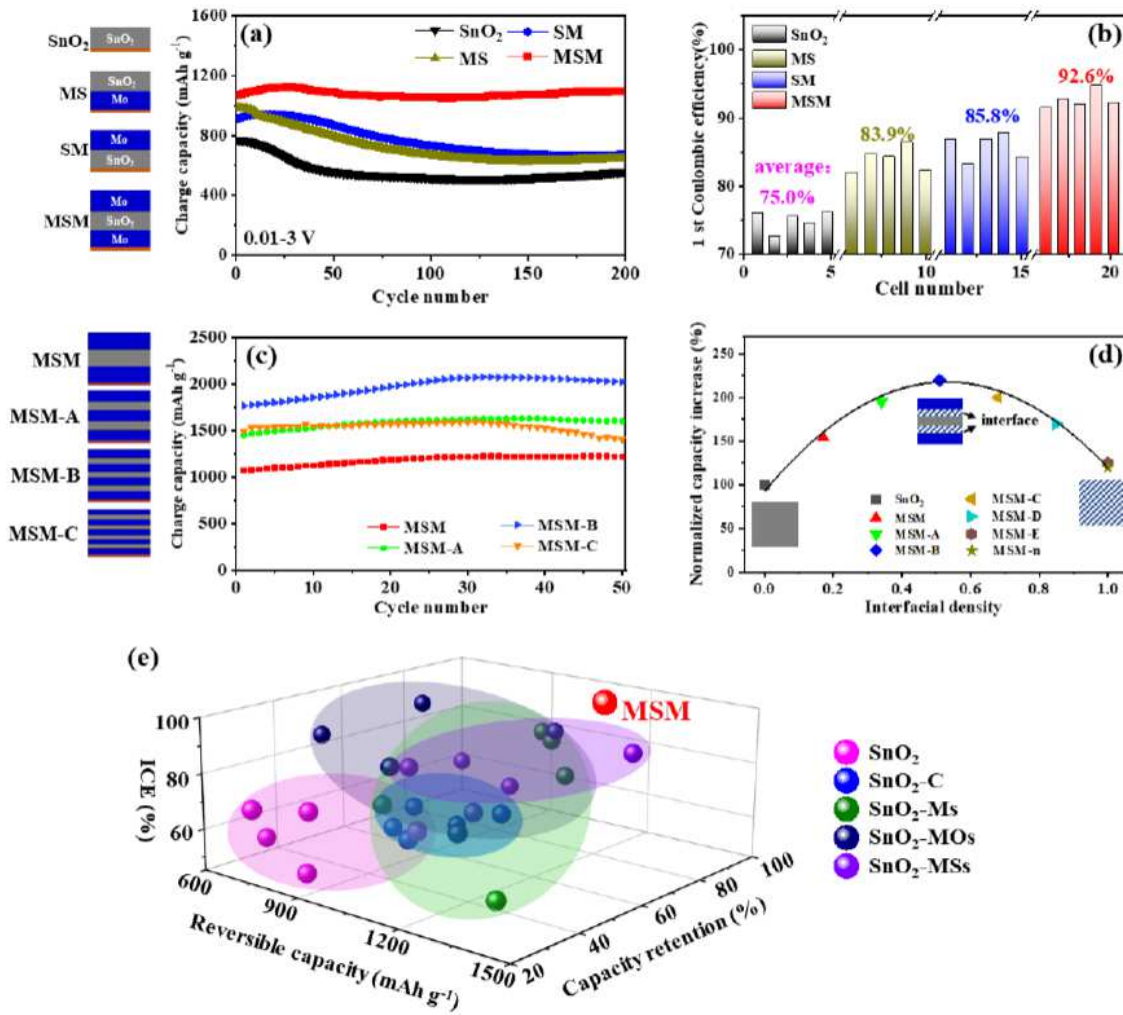


Figure 1

Highly reversible and stable Li storage properties of SnO₂ Mo electrodes in half cells. (a) Comparison of charge capacity. (b) Summary of the ICEs from every five cells for SnO₂, SM, MS and MSM electrodes. (c) Cycling performance of MSM A, MSM B and MSM C electrodes in the initial 50 cycles. (d) The relationship between normalized capacity increase and interfacial density. The charge capacity of each electrode is taken from the 5th cycle. The dotted lines represent the capacity increase calculated from the fitting curves. (e) The reversible capacities, capacity retentions after 200 cycles and ICEs of SnO₂ based anodes for LIBs reported in the recent literatures, including the pure SnO₂,^{25, 26, 29, 31} SnO₂ C,^{27, 28, 34, 36} SnO₂ Metals (SnO₂ Ms),^{32, 33, 39, 41} SnO₂ Metal oxides (SnO₂ MOs)^{33, 37, 38, 43, 45} and SnO₂ Metal sulfides (SnO₂ MSs)^{30, 31, 42, 44, 46}. The red sphere represents the average electrochemical performance of the MSM electrode.

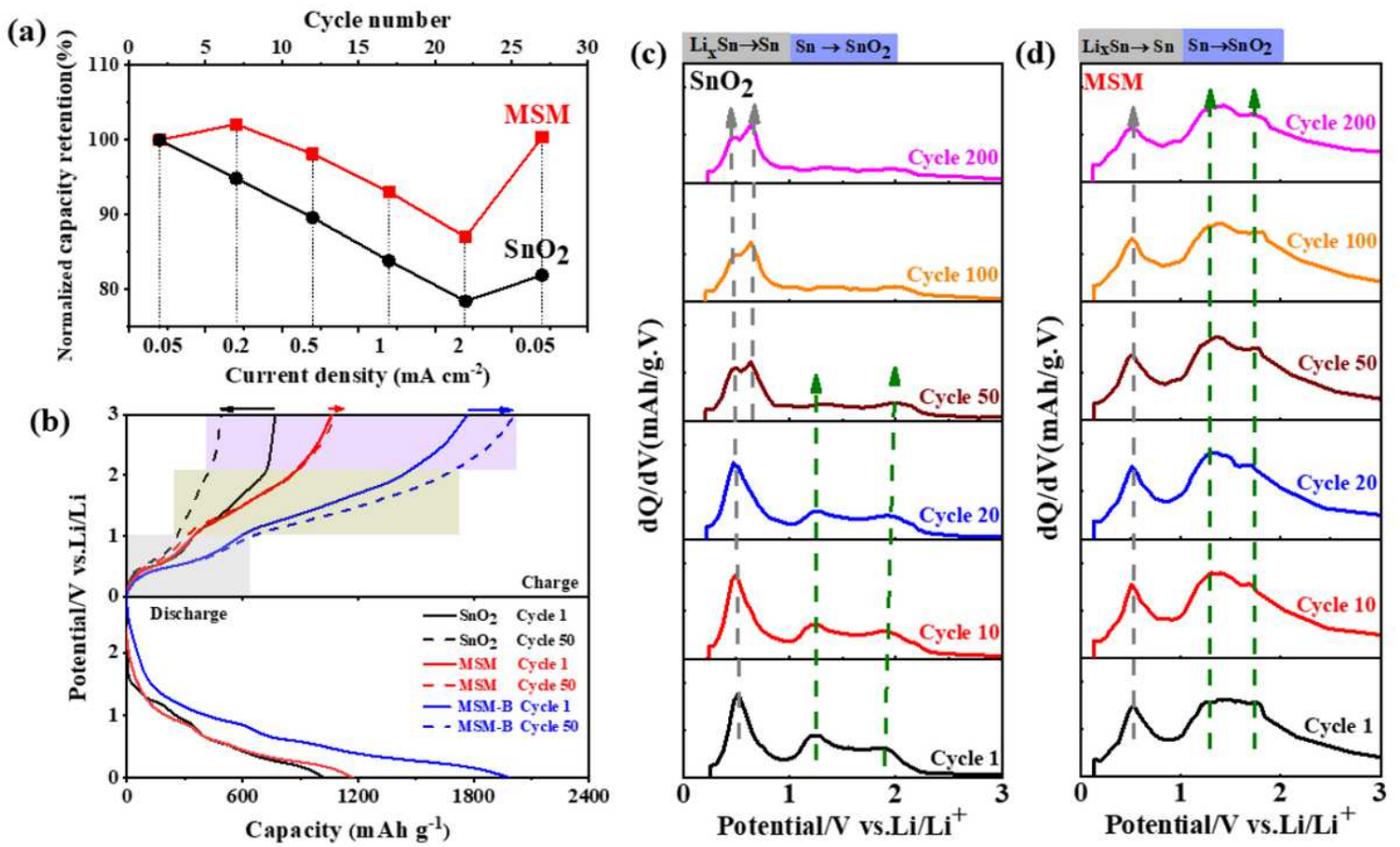


Figure 2 Comparison of the rate capabilities and reaction reversibility for the SnO₂ and MSM electrodes. (a) Rate capabilities of SnO₂ and MSM electrodes. (b) Charge discharge profiles of SnO₂, MSM and MSM B electrodes at the 1st and 50th cycles. (c, d) Differential charge capacity vs. voltage curve of SnO₂ and MSM electrodes at the 1st, 10th, 20th, 50th, 100th and 200th cycles.

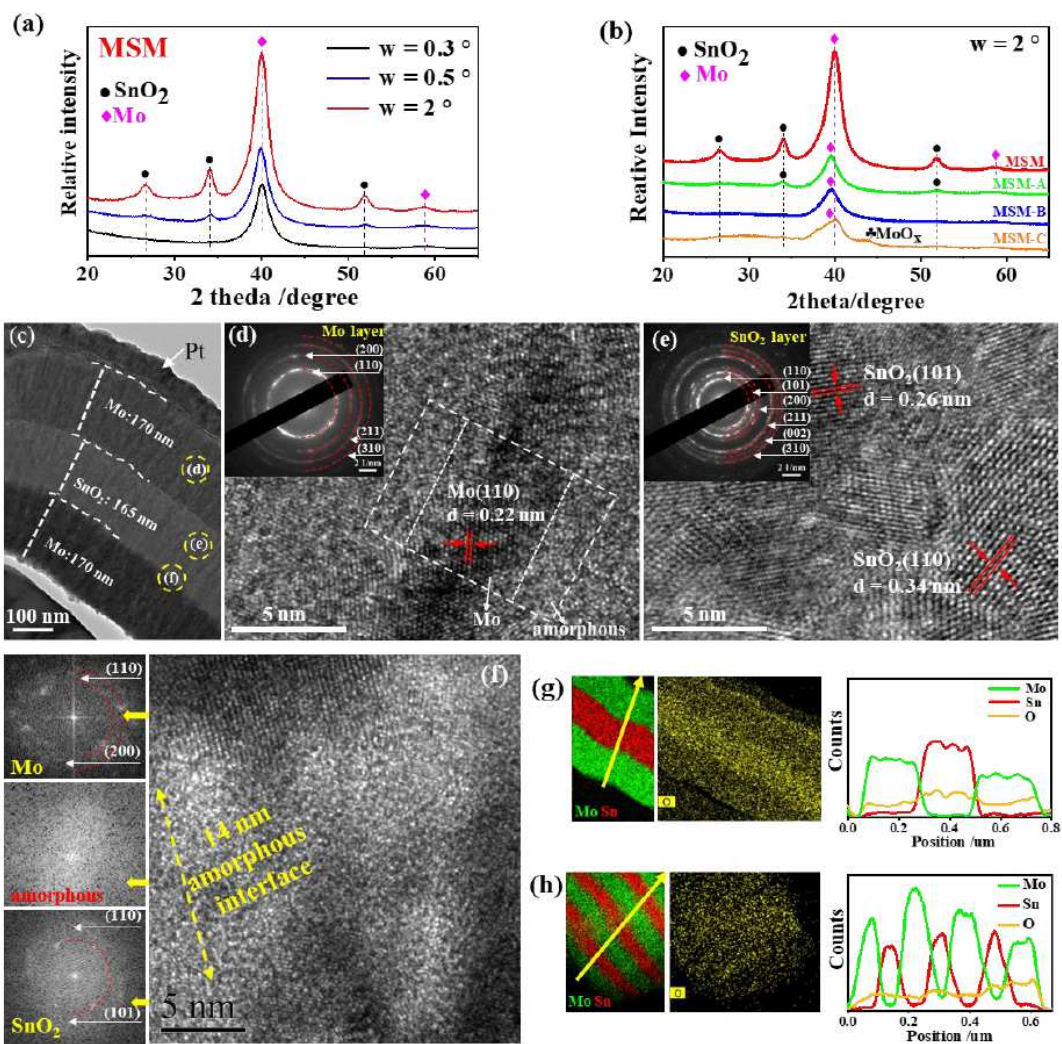


Figure 3

GI-XRD and FIB-TEM characterizations of the structure and cross sectional morphology of MSM, MSM-A, MSM-B and MSM-C. (a) GI-XRD patterns of MSM with the incident angle of 0.3° , 0.5° and 2.0° . (b) GI-XRD patterns of MSM, MSM-A, MSM-B and MSM-C with the incident angle of 2° . (c-g) TEM observation of MSM. (c) Typical FIB-TEM image of cross-sectional morphology. (d, e) HRTEM images of the Mo and SnO₂ layers, insets in (d) and (e) are the corresponding SAED images. (f) HRTEM image at the interface between Mo and SnO₂ layers, and FFT images of corresponding regions. (g, h) EDS mapping and line-scan images of Sn, Mo and O elements for MSM and MSM-B.

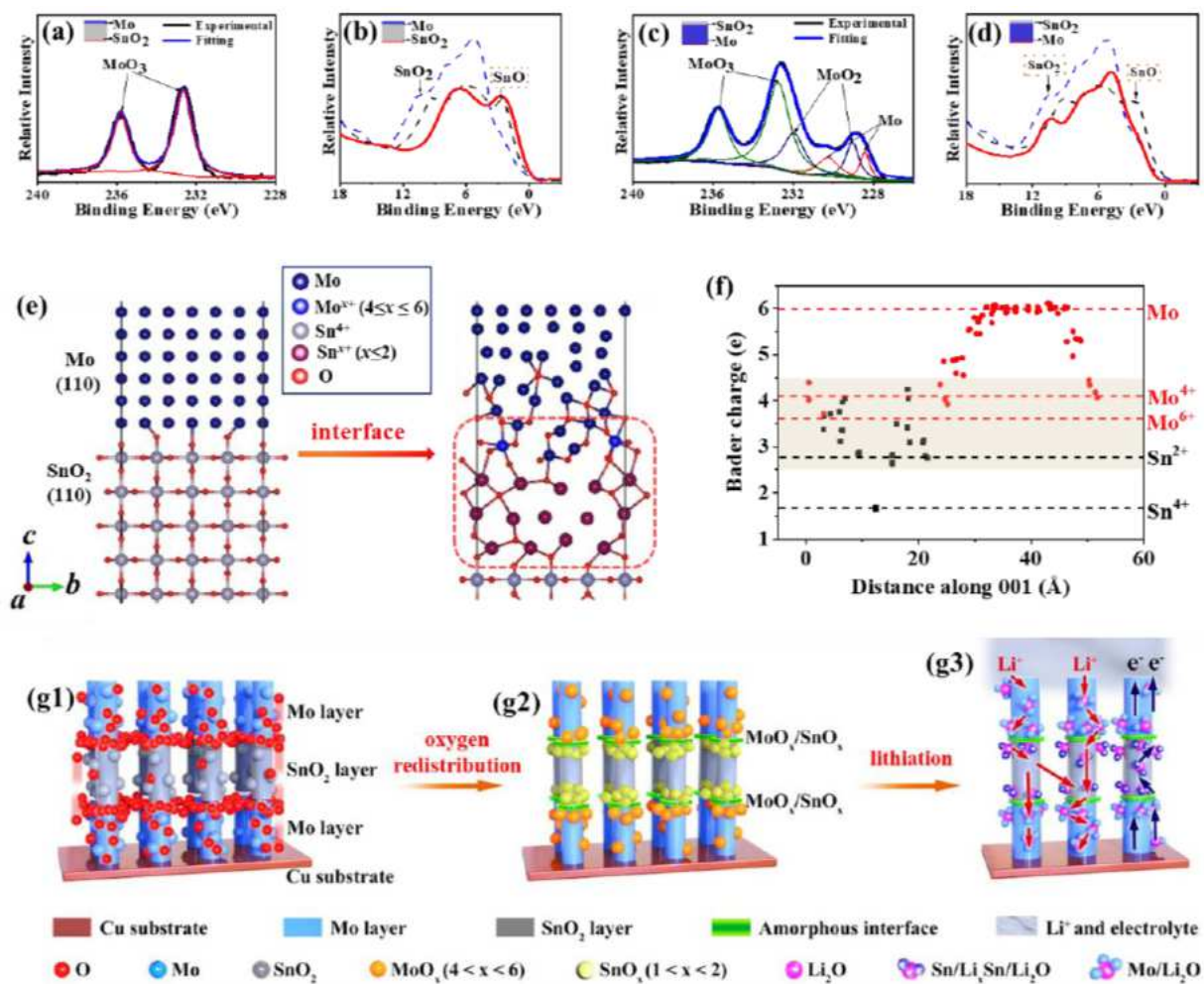


Figure 4

XPS analysis and DFT calculations of valence states and charge distributions at the interfaces of MSM. (a-d) XPS spectra at the interfaces of MSM. (a) Mo 3d at the up side of interface in MSM. (b) Valence band Spectrum of Sn 3d at the up side of interface in MSM. (c) Mo 3d at the down side of interface in MSM. (d) Valence band Spectrum of Sn 3d at the down side of interface in MSM. (e) Crystal structure of Mo, SnO₂ and the interface viewed along [001] direction. (f) Distribution of valence states of Sn and Mo atoms at the hetero interface in MSM. (g) Schematic showing the redistribution of O and the rapid transfer process of electrons/ions in MSM.

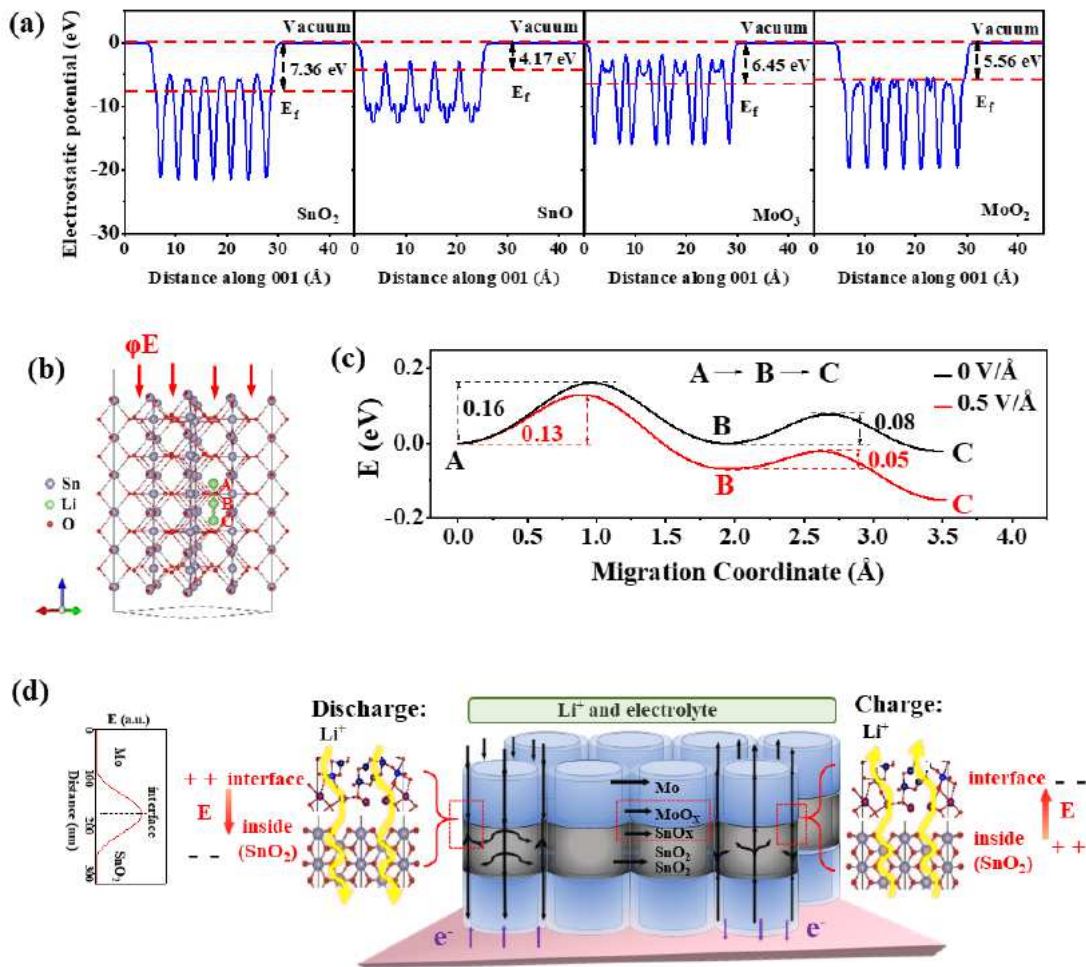


Figure 5

DFT calculations of the Li^+ transfer dynamics boosted by induced electric field effect (E). (a) Calculated electrostatic potential of SnO_2 , SnO , MoO_3 , and MoO_2 , respectively. (b) Crystal structure of SnO_2 with three Li^+ intercalated at A, B, and C sites. (c) Calculated diffusion barrier of Li^+ from A→B and B→C along the electric field. (d) Schematic diagram of the effect of E and the mechanism of boosted charge transfer within MSM.

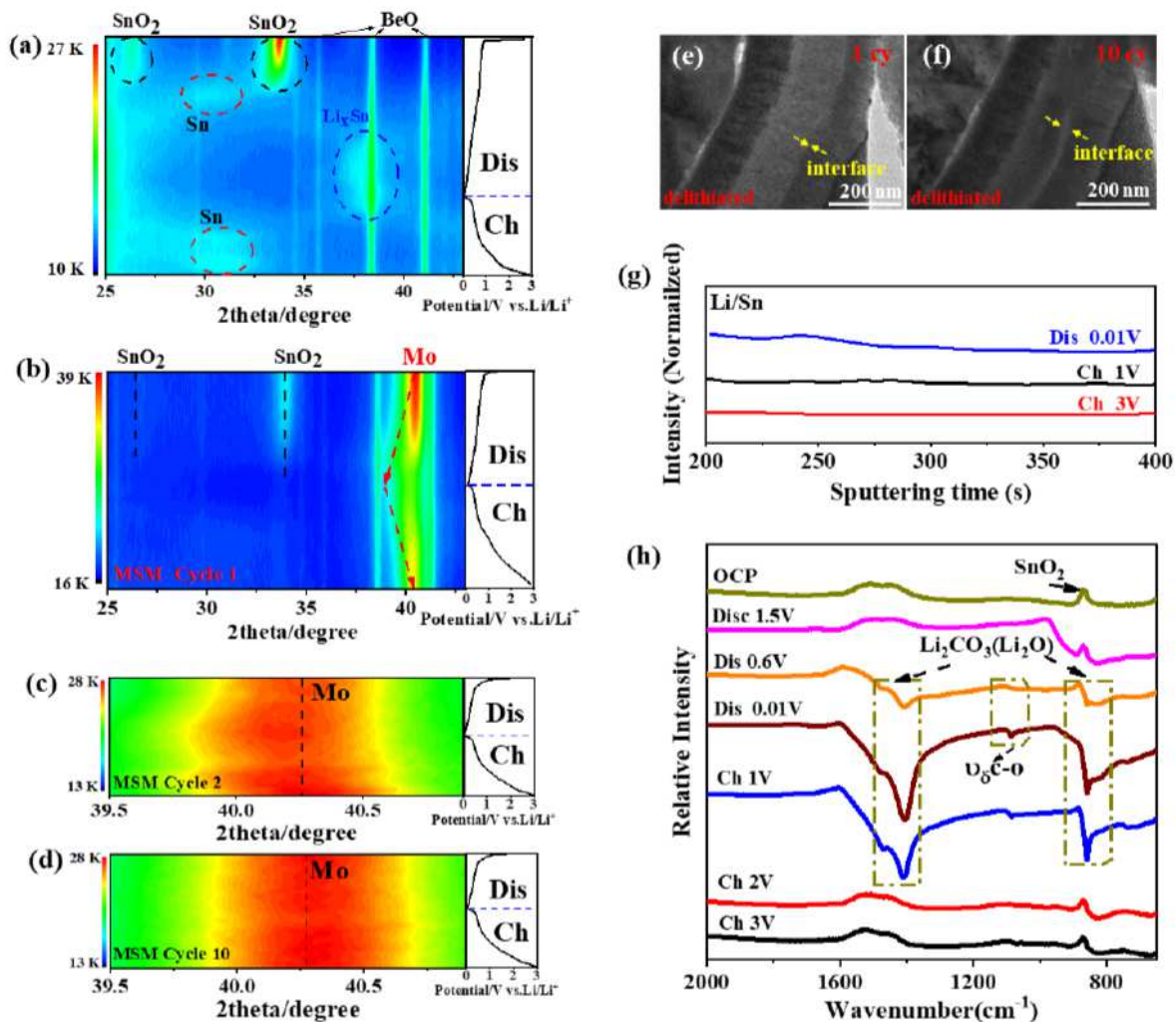


Figure 6

In/ex-situ observations of morphology and phase evolution of MSM electrode during lithiation/delithiation processes. (a-d) Contour plots of in-situ XRD patterns against the voltage for the SnO₂ and MSM electrodes. (a) SnO₂ electrode during the 1st cycle. (b-d) MSM electrode during the 1st cycle (b), 2nd cycle (c) and 10th cycle (d). (e, f) In situ TEM observation of MSM electrode at the fully delithiated status in the 1st cycle (e) and 10th cycle (f). (g) TOF-SIMS characterization for Li/Sn depth profiles as discharged to 0.01 V, charged to 1V and 3V in the 1st cycle. (h) Ex-situ FTIR spectra at seven different states during the 1st cycle, namely OCP, discharged to 1.5V, 0.6V and 0.01 V, recharged to 1V, 2V and 3.0 V.

Supplementary Files

This is a list of supplementary files associated with this preprint. Click to download.

- [SupplementaryInformationAchievingover90XinitialCoulombicefficiencyandhighlystableListorageinSnO2byconstructinginterfacialoxygenredistributioninm](#)
- [VideoS1.mp4](#)
- [VideoS2.mp4](#)